

Report on

Computational Modeling of Small Energy Harvester Subjected to Aero-elastic Instabilities

THESIS

Submitted in partial fulfillment of the requirements of
BITS F423T, Thesis

by

Jalaj Maheshwari (2011A4TS224G)

under the supervision of

Dr. Murali Damodaran

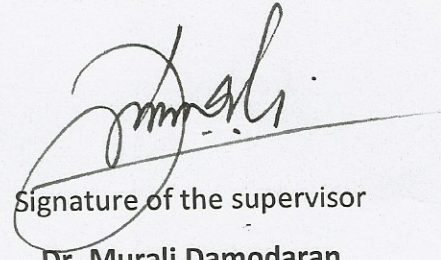
Professor, Discipline of Mechanical Engineering, IIT Gandhinagar



BIRLA INSTITUTE OF TECHNOLOGY AND SCIENCE, PILANI
K.K. BIRLA GOA CAMPUS

CERTIFICATE

This is to certify that the thesis entitled "**Computational Modeling of Small Energy Harvester Subjected to Aero-elastic Instabilities**" is submitted by Jalaj Maheshwari, ID No. 2011A4TS224G, in partial fulfillment of the requirements of **BITS F423/ BITS F421T**. This thesis embodies the work done by him under my supervision.



Signature of the supervisor
Dr. Murali Damodaran

Date: 11 May 2015

Professor
Indian Institute of Technology Gandhinagar
Ahmedabad-382424, Gujarat, India

Abstract



Title of document: COMPUTATIONAL MODELING OF SMALL ENERGY HARVESTER SUBJECTED TO AERO-ELASTIC INSTABILITIES

Supervisor: Professor Murali Damodaran
Discipline of Mechanical Engineering

Semester: Second Year: 2014/2015

Name: Jalaj Maheshwari ID No.: 2011A4TS224G

Aero-elastic instability or flutter, in particular, is an undesirable phenomena experienced by bodies exposed to cross wind and can cause serious damage due to fluid-structure interaction especially in airplane wings. However, this property of aero-elastic instability can be used on a small body to harness energy from the cross wind. Computational modelling of a small energy harvesting device is carried out to study the effects of wind on the body, which can be further used to produce electricity. The present study shows the aerodynamic response of a T-shaped flat plate with a tip mass. Piezoelectric strips are placed on either side of the plate near the region where the plate is fixed. The bottom side of both piezoelectric bodies is given zero voltage. When the harvester body flutters, mechanical strain is generated in the harvester, which causes strain in the piezoelectric bodies, thus, generating a voltage in each piezo body. The complex fluid-structure interaction requires coupling of fluid flow around the harvester, with the structural model. Computational fluid dynamics based on the incompressible Navier-Stokes equation and computational structural analysis based on the Lagrangian equation of motion is carried out using a partitioned solving approach in ANSYS.

Keywords: Fluid-Structure Interaction, Energy Harvester, Flutter, Piezoelectricity.

Acknowledgements

I would like to express my deepest gratitude to Professor Murali Damodaran for the patience, guidance, encouragement and advice he has provided throughout my time under his supervision. I have been extremely lucky to have a supervisor who has shown the deepest of interests in my work and who has responded to my queries and doubts so promptly. His constant support, deep understanding and interest in the field of Fluid Dynamics, Computational Fluid Dynamics and Numerical Methods are of indispensable value and help. I would like to acknowledge his efforts in pushing me to my limits and in making me think freely and broadly in every aspect. He is one of the best mentors I have had and it was a privilege to have worked under his guidance.

I would like to thank my colleagues and friends at the High Performance Computing Lab at the Indian Institute of Technology Gandhinagar for their continuous support throughout my association with the institute. I would like to thank Mr. Akshay Kanoria and Mr. Jay Sudani for their technical and inspirational support throughout my time at the institute. I would also like to acknowledge the IT department of IIT Gandhinagar in promptly addressing any technical issues and providing constant technical support. I would like to dedicate this thesis project to my loving and supportive parents and my dear ones who have been with me through my various stages of life.

Table of Contents

Abstract.....	ii
Acknowledgements.....	iii
Table of Contents	iv
Table of Figures	v
Table of Tables.....	vi
Nomenclature.....	vii
Chapter 1 : Introduction.....	1
1.1 Background and Motivation.....	1
1.2 Introduction to Fluid-Structure Interaction	2
1.2.1 One-Way FSI.....	2
1.2.2 Two-Way FSI.....	3
1.3 Objective of the current study	4
Chapter 2 : Mathematical and Computational Modeling.....	5
2.1 Governing Equations	5
2.1.1 Fluid-Structure Physics Governing Equations	5
2.1.2 Geometric Conservation Equation.....	7
2.1.3 Fluid-Structure Interaction Working Algorithm.....	7
2.1.4 Piezoelectric Governing Equation.....	10
2.2 Discretization of Computational Domain.....	11
Chapter 3 : Results and Discussions	17
3.1 Spatial Grid Convergence	17
3.2 Computed Flow past the Energy Harvester for Reynolds Number Equal to 0.89×10^5 . 20	20
3.3 Computed Flow past the Energy Harvester for Reynolds Number Equal to 2.28×10^5 . 29	29
Chapter 4 : Conclusion and Future Work	38
References	40
Appendix.....	43

Table of Figures

Figure 2.1: 2-Way FSI, (a) Gauss-Seidel sub-iterative FSI, (b) FSI computation flow chart	9
Figure 2.2: Schematic of harvester model.....	11
Figure 2.3: Harvester dimensions, (a) Side view, (b) Front View, (c) Top View	12
Figure 2.4: Computational domain with boundary conditions	12
Figure 2.5: Structural boundary conditions	13
Figure 2.6: Overview of the computational domain, (a) Harvester surface mesh, (b) Surface mesh on thin plate,.....	16
Figure 3.1: Spatial grid convergence, (a) Tip deformation variation for structural mesh, (b) Side force variation for fluid mesh	19
Figure 3.2: (a) Pressure and (b) Vorticity contours for aluminium harvester at specified time instants t for wind speed of 9m/s.....	21
Figure 3.3: (a) Pressure and (b) Vorticity contours for structural steel harvester at specified time instants t for wind speed of 9m/s.....	22
Figure 3.4: (a) Aluminium and (b) Structural Steel wall shear contours at specified time instants t for wind speed of 9m/s.....	25
Figure 3.5: (a) Aluminium and (b) Structural Steel von Mises stress contours at specified time instants t for wind speed of 9m/s (inset, stress on piezoelectric strip)	27
Figure 3.6: Variation of parameters for different materials at 9m/s, (a) Tip displacement, (b) Maximum strain, (c) Piezoelectric voltage from piezo body-1, (d) Piezoelectric voltage from piezo body-2.....	28
Figure 3.7: (a) Pressure and (b) Vorticity contours for aluminium harvester at specified time instants t for wind speed of 23m/s.....	30
Figure 3.8: (a) Pressure and (b) Vorticity contours for structural steel harvester at specified time instants t for wind speed of 23m/s.....	32
Figure 3.9: (a) Aluminium and (b) Structural Steel wall shear contours at specified time instants t for wind speed of 23m/s.....	34
Figure 3.10: (a) Aluminium and (b) Structural Steel von Mises stress contours at specified time instants t for wind speed of 23m/s (inset, stress on piezoelectric strip)	35
Figure 3.11: Variation of parameters for different materials at 23m/s, (a) Tip displacement, (b) Maximum strain, (c) Piezoelectric voltage from piezo body-1, (d) Piezoelectric voltage from piezo body-2.....	37

Table of Tables

Table 2.1: PZT-5A electromechanical and mechanical properties	14
--	----

Nomenclature

<i>Symbol</i>	<i>Description</i>
\vec{U}	Velocity of Fluid
ρ	Fluid Density
p	Static Pressure
$\vec{\tau}$	Stress Tensor
\vec{f}	Body Force
$[M]$	Structural Mass Matrix
$[C]$	Structural Damping Matrix
$[K]$	Structural Stiffness Matrix
$\ddot{u}(t)$	Nodal Acceleration
$\dot{u}(t)$	Nodal Velocity
$u(t)$	Nodal Displacement
$F_{fluid}(t)$	Fluid Pressure Force
t	Time
\dot{u}_s	Velocity of Structural Domain
\dot{u}_f	Velocity of Fluid Domain
σ_s	Structural Stress
σ_f	Fluid Stress
n_s	Structural Normal Vector at Fluid-Solid Interface
n_f	Fluid Normal Vector at Fluid-Solid Interface
u_s	Displacement of Structural Domain
u_f	Displacement of Fluid Domain
ϕ	General Scalar

Symbol	Description
\vec{u}_g	Velocity of Moving Mesh
Γ	Diffusion Coefficient
U_t^F	Fluid Parameters at time t
p_t^F	Fluid Pressure at time t
U_t^S	Structural Parameters at time t
D	Electrical Displacement Field Vector
ε	Strain Vector
E	Applied Electric Field Vector
σ	Stress Vector
e^σ	Dielectric Permittivity
d^d	Piezoelectric Coefficient at constant Electric Field
d^c	Piezoelectric Coefficient at constant Stress
s^E	Elastic Compliance
L	Height of Harvester Body
r	Mesh Refinement Ratio
h_1, h_2	Mesh sizes
C	Order of Convergence
f_1, f_2, f_3	Computed Variables
P_r	Asymptotic Value
F_s	Factor of Safety
ε	Relative Error
N	Cell Count

Chapter 1 : Introduction

1.1 Background and Motivation

The demand for energy is commensurate to the population of the earth. Over the past 25 years, the population, and subsequently, the energy consumption of the world is increasing. These rapidly increasing energy demands are primarily met by use of conventional sources of energy, which account for producing nearly 63% of the world's energy. Although these sources fulfill the energy demands of the world, these fossil fuels are depleting and will exhaust in the near future. There is a dire need to substitute these conventional sources with other renewable sources of energy. Thus, energy harvesting through renewable sources of energy has been an active research area since demand for these sources is on the rise. Several recent studies have researched the possibility of the use of renewable sources to produce energy as opposed to the conventional non-renewable sources of energy. Wind energy is one such natural renewable source that can be tapped efficiently to produce power. This has been centered predominantly on the use of wind turbines to produce power on a large scale. However, bodies subjected to cross wind are susceptible to aero-elastic instability or flutter in particular, which is an undesirable phenomenon and can cause serious damage due to the fluid-structure interaction, especially in airplane wings and bridges. These vibrations from the fluid flow, although undesirable, can be used to generate electricity. Studies have aimed at producing electricity from aero-elastic instability induced by the Karman vortex street as done by Wang et al. [1]. Further, experimental studies have been carried out to determine the net energy output from a small harvester by incorporating the use of permanent magnets, as demonstrated by Park et al. [2] where the movement of permanent magnets is used to induce a current in electrical coils placed adjacent to the magnets.

Research based on the use of piezoelectric polymer strips for energy harvesting has been conducted extensively. The oscillation of piezoelectric strips has been used to produce energy by Taylor et al. [3], Liya et al. [4], Sundarajan et al. [5], Abdelkefi et al. [6], Ali et al. [7], Kwon [8] and Bryant and Garcia [9]. Taylor et al. [3] have demonstrated the use of the regular trail of travelling vortices behind a buff body to strain the piezoelectric strips through flow of water in

a river. Abdelkefi et al. [6] have demonstrated the use of a unimorph piezoelectric cantilever beam with a square cross section tip mass to produce electricity whereas Gallina and Benasciutti [10] have used bimorph piezoelectric cantilever beam to determine the net electric output from the flutter of the beam. Moreover, they have demonstrated the output generated from different shaped of cantilever beams. Ali et al. [7] have proposed and studied the energy generated through different shapes of the tip mass.

1.2 Introduction to Fluid-Structure Interaction

Fluid-structure interaction is the interaction of a deformable or a movable structure due to internal or external fluid flow. In the numerical simulation of fluid-structure interactions, the fluid equations and the structural equations are solved simultaneously in order to understand the physics and the behavior of a body subjected to fluid flow. The typical applications of fluid-structure interaction are included in aerospace engineering in airfoil flutter, turbine engines, helicopter fluttering and parachute FSI and in automotive engineering in study of heat exchangers and heating and cooling of automobile components. Civil engineering finds usage of FSI in the interaction of buildings and bridges with cross wind. This phenomenon is also used to study the flow of fluids through valves, in the regulation of pressure and in fuel injection. The applications of FSI are not limited to engineering and find their usage in biomedical studies as well, some of which are intravenous fluid flow and flow through arteries and aortic valves. Depending on the type of coupling, fluid-structure interaction can be further divided into two main categories.

1.2.1 One-Way FSI

A one-way fluid-structure interaction simply describes the mapping of physical properties from analysis of the fluid model, to the finite elements model in structural. Here, the pressure forces generated by the fluid flow over the body are computed and mapped to the structural equations to determine the results of the fluid-structure interaction. The fluid and the structural models need not rely on matching meshes as the structural analysis results are not used in the fluid equations to compute further values. Moreover, in one-way FSI, there is no deformation of the mesh in the fluid region. One-way FSI simulations are primarily used to

determine the action of fluid flow over a particular structure and to study the behavior of the structure due to forces generated by the fluid flow.

1.2.2 Two-Way FSI

A two-way fluid structure interaction co-simulates the fluid flow solver and the finite element structural solver in an iterative loop. The pressure forces due to the fluid flow are calculated, which are further used in the structural equations to calculate the deformation of the body under study. The structural deformation results are then used in the fluid equations to further compute the pressure forces at that deformed moment, which are consequently used in structural equations again to calculate further deformation of the body under study. This is an iterative loop where the fluid and the structural equations are solved one after the other to compute the interaction of a solid body in a region of fluid flow. As the structural deformation takes place, the mesh in the fluid region also has to be deformed to account for the previously calculated structural deformation. The fluid and the structural meshes need to match for correct mapping of physics in both the fluid and finite element solver. Thus, the fluid equations, structural equations and the mesh deformation are calculated simultaneously in order to study the behavior of the body in a region of fluid flow. This iterative procedure is continued until convergence is reached or the time over which the simulation has to be carried out is completed.

1.3 Objective of the Current Study

The prime focus of the current study is to study the fluid-structure interaction of the harvester body subjected to a certain wind speed and the corresponding net voltage generated from the piezoelectric body attached to the harvester model. As part of the study, the nature of oscillations of the harvester model is studied for different wind speeds corresponding to laminar as well as turbulent flows. For the given harvester size, the Reynolds number corresponding to different speeds determine whether the flow is laminar or turbulent. For turbulence modeling, the Spalart-Allmaras turbulence model is used as the harvester is to be kept in free stream conditions. The details of the computational approach are provided in the subsequent chapters. Further, the material of the harvester body is changed to study the change in the nature of the oscillations. One of the other motives is to study the flow field around the harvester body as it oscillates at a certain wind speed. The structural parameters such as the displacement of the tip mass and the stress and strain generated are monitored for each case with different wind speed and harvester material. Post the fluid-structure analysis, the net voltage generated from the piezoelectric bodies attached to the harvester is found commensurate to the strain produced in the bodies. The voltage output for each case is studied and the respective graphs are plotted. This study will lay the foundation for further studies such as power output from an array of harvesters, layout of array of harvesters and so on.

Chapter 2 : Mathematical and Computational Modeling

This chapter focuses on the salient aspects of the computational modeling of the free stream flow past a small energy harvester using laminar and turbulent models for subsequent cases. Section 2.1 deals with the mathematical equations pertaining to the computational model. Further sections discuss the discretization of the computational model and its salient features.

2.1 Governing Equations

The equations pertinent to the computational modeling which are solved over the simulation are discussed in the following sections. The subsequent sections explain the equations and the working of the fluid solver and the structural solver and the exchange of data between the two in fluid-structure interaction. Further, the piezoelectric governing equations are incorporated into the study to determine the voltage output.

2.1.1 Fluid-Structure Physics Governing Equations

The complex fluid-structure interaction modeling is carried out using a partitioned solving approach, where the discretization of the mesh and the numerical algorithm for the fluid and structural solver are different. Within the framework of ANSYS, the fluid solver uses a finite volume discretization method, whereas the structural solver uses a finite element discretization method. Here, the incompressible Navier-Stokes equation for fluid flow analysis and the Euler-Lagrangian equation of motion for structural analysis are solved separately as opposed to the monolithic solving approach, where both the fluid and structural equations are solved simultaneously. For cases where the calculated Reynolds number is below 2×10^5 , the laminar model is used. However, for cases where the calculated Reynolds number is above this value, the one equation Spalart-Allmaras turbulence model [11] is used in the computational modeling.

$$\rho \left(\frac{d}{dt} \int_V \vec{U} dV + \int_S \vec{U} \cdot \vec{n} dS \right) = - \int_S p \vec{n} dS + \int_S \vec{\tau} \cdot \vec{n} dS + \rho \int_V \vec{f} dV \quad (2.1)$$

$$[M] \{ \ddot{u}(t) \} + [C] \{ \dot{u}(t) \} + [K] \{ u(t) \} = F_{fluid}(t) \quad (2.2)$$

Here, \vec{U} is the velocity of fluid, ρ is the fluid density, p is the static pressure, $\vec{\tau}$ is the stress tensor, \vec{f} represents the body forces, $[M]$, $[C]$ and $[K]$ are the structural mass, damping and stiffness matrix respectively, $\ddot{u}(t)$, $\dot{u}(t)$ and $u(t)$ are the nodal acceleration, velocity and displacement vectors respectively and $F_{fluid}(t)$ represents the fluid pressure force computed by the incompressible Navier-Stokes equation.

In the partitioned approach, the fluid and the structural meshes are discretized separately. Hence, there is a large margin of error while mapping data from the fluid solver to the structural solver and vice-versa. At each successive time step, due to the action of pressure forces computed from Eq. (2.1), the structural body is deformed and the displacement is calculated by Eq. (2.2). The interface that divides the fluid domain and the structural domain is not known beforehand, and keeps changing with time. Thus, the partitioned solving approach requires the tracking of the structural deformation at each time step which can be highly error prone in the computational modeling. A fluid-solid interface is defined at the boundary of the structural domain. This interface needs to be tracked at every time step in order to map data between the fluid and structural solver. As depicted by Hou et al. [12] and Baek and Karniadakis [13], the conditions at the fluid-solid interface are given as:

$$\dot{u}_s = \dot{u}_f \quad (2.3)$$

$$\sigma_s n_s = \sigma_f n_f \quad (2.4)$$

where, \dot{u}_s is the velocity associated with the structural domain, \dot{u}_f is the velocity associated with the fluid domain, σ_s is the structural stress, σ_f is the fluid stress, n_s and n_f are the normal vectors corresponding to the structural and fluid domain at the fluid-solid interface pointing outward. Eq. (2.3) and Eq. (2.4) are further reduced by concluding that the structural and fluid domains share the same interface and hence:

$$u_s = u_f \quad (2.5)$$

where, u_s is the displacement in the structural domain and u_f is the displacement in the fluid domain. Thus, the structural deformation and the fluid deformation conditions at the fluid-solid interface govern the FSI formulation in computational modeling.

2.1.2 Geometric Conservation Equation

Due to the deformation of the fluid and the structural domains, the physics at each successive time step needs to be mapped from the fluid solver to the structural solver and vice-versa efficiently. ANSYS works on conforming mesh method algorithm. The conforming-mesh method tracks the position of the fluid-solid interface and enforces Eq. (2.4) and Eq. (2.5) on it. Therefore, an additional equation is solved at each time step apart from the fluid dynamics Eq. (2.1) and structural dynamics Eq. (2.2) which is the geometric conservation law which is given by:

$$\frac{d}{dt} \int_V \rho \phi dV + \int_{\partial V} \rho \phi (\vec{U} - \vec{u}_g) \cdot d\vec{A} = \int_{\partial V} \Gamma \nabla \phi \cdot d\vec{A} \quad (2.6)$$

where, ϕ is any general scalar, \vec{u}_g is moving mesh velocity and Γ is diffusion coefficient. This mesh conservation equation ensures the coordination of the data transferred between the fluid solver and the structural solver. This geometric conservation equation is followed at every time step.

2.1.3 Fluid-Structure Interaction Working Algorithm

The structural surface mesh and the fluid volume mesh do not conform completely. Hence, the margin for error in such a calculation is large. Thus, for both structural and the fluid solvers, the geometrical conservation equation given by Eq. (2.6) is followed. According to Hou et al. [12], the fluid mesh deals with the physics around the fluid-solid interface whereas the structural mesh deals with load bearing areas which are usually away from the fluid-solid interface. Thus, there is a mismatch in the fluid and the structural meshes at the interface and may even contain gaps. This mismatch in the meshes at the fluid-solid interface can result in improper

data transfer between the fluid and the structural solver, thus providing incorrect results. A point match method is employed in most commercial software, which takes into account the incongruence in the meshes. Using this method, a fluid mesh point and a structural mesh point are identified and matched. The displacement of a structural mesh point is computed and transferred to the fluid mesh point through these matched points. Once the displacement of all such matched points is calculated, the displacement of all other points is calculated through interpolation. Similarly, the fluid pressure forces computed by the fluid solver are transferred to the structural solver through these matched points.

All these calculations take place at the fluid-solid interface where the physics of the system is changing. Thus, a fluid-structure interaction problem works in an iterative loop, where the fluid equation, Eq. (2.1), structural equation, Eq. (2.2) and the mesh conservation equation, Eq. (2.6), are solved one after the other. Further, the fluid and the structural computation must have further sub-iterations defined as the sequential computation can likely become unstable as shown by Wood et al. [14]. To ensure a strong coupling between the fluid and the structural fields using the partitioned approach, full convergence at each sub-iteration for every time step should be met, as proposed by Farhat and Lesoinne [15].

The partitioned fluid-structure interaction is implemented using the Gauss-Seidel method. This iterative scheme strongly couples the fluid and the structural solvers to compute the fluid-structure interaction. The structural displacement $u(t)$ is used to gauge the motion of the fluid-solid interface and a deformed mesh is generated over the fluid domain. Further, the fluid domain mesh velocity \vec{u}_g is computed. Corresponding to the new fluid domain, the pressure and velocity fields are calculated which satisfy the condition at the moving fluid-solid interface as given by Eq. (2.5). The fluid pressure is then transferred to the structural discretization to calculate the updated structural loading. This load is then used to compute the structural parameters namely acceleration $\ddot{u}(t+1)$, velocity $\dot{u}(t+1)$ and the displacement $u(t+1)$. The 2-Way FSI using the Gauss-Seidel method is shown in Figure 2.1(a). The complete overview of the 2-Way FSI is explained in the flow chart as in Figure 2.1(b).

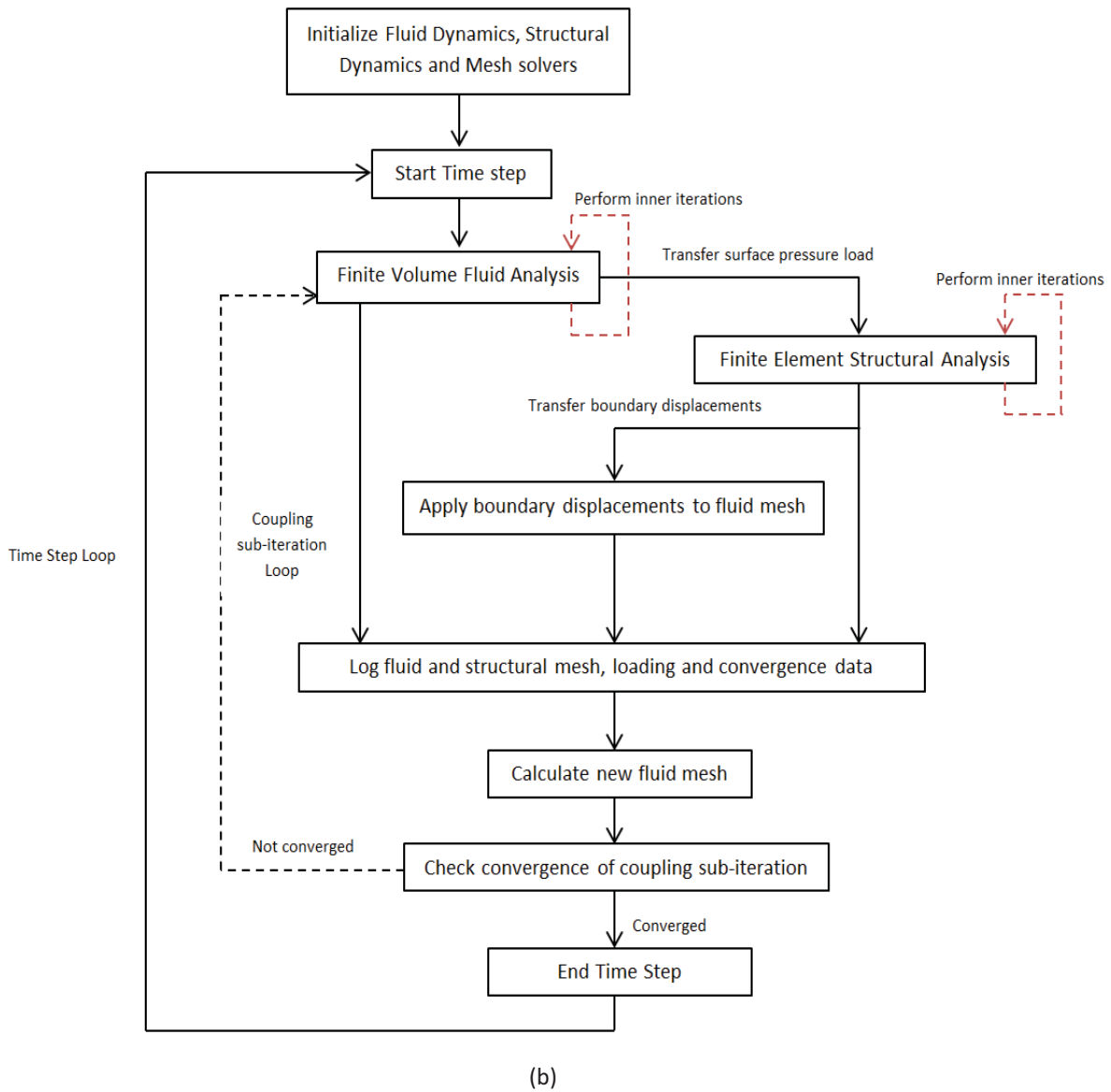
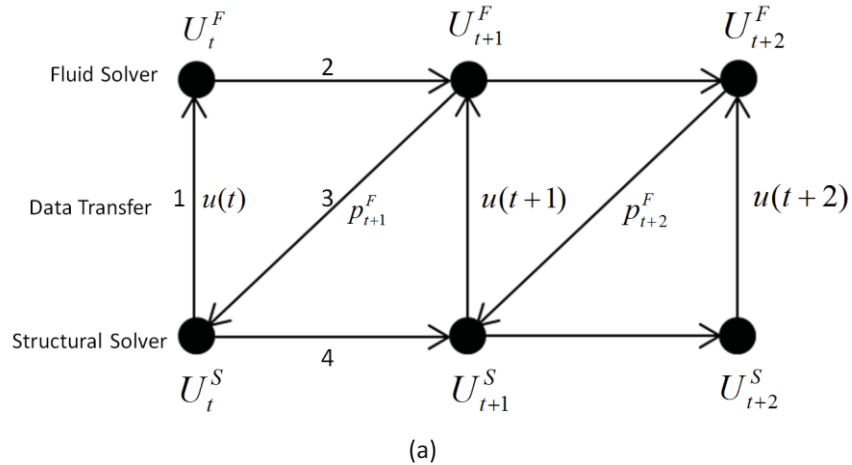


Figure 2.1: 2-Way FSI, (a) Gauss-Seidel sub-iterative FSI, (b) FSI computation flow chart

In Fig. 2.1(a), U_t^F represents the fluid parameters at time t , which include the fluid pressure p_t^F and the fluid velocity field. Also, U_t^S represents the structural parameters at time t which includes the acceleration $\ddot{u}(t)$, velocity $\dot{u}(t)$ and the structural displacement $u(t)$. In Fig. 2.1(b), the complete working of a 2-Way FSI is shown as followed in a partitioned based solving approach.

2.1.4 Piezoelectric Governing Equation

A typical characteristic of a piezoelectric element is that it generates an electrical voltage when mechanical stress or pressure is acted upon it and vice-versa. The constitutive relation for any piezoelectric material, given by the IEEE Standard [16] is as follows:

$$\begin{bmatrix} D \\ \varepsilon \end{bmatrix} = \begin{bmatrix} e^\sigma & d^d \\ d^c & s^E \end{bmatrix} \begin{bmatrix} E \\ \sigma \end{bmatrix} \quad (2.7)$$

where, D represents the electrical displacement field vector, ε represents the strain vector, E is the applied electrical field vector and σ is the stress vector. The dielectric permittivity e^σ , piezoelectric coefficients, d^d and d^c , and the elastic compliance s^E are the piezoelectric constants. The electrical displacement vector depicts the effect of free charges per unit length of the piezoelectric material. The piezoelectric coefficients d^d and d^c represent the electrical displacement per unit stress at constant electrical field and the strain per unit electrical field at constant stress respectively. The dielectric permittivity is calculated at constant stress and the elastic compliance is calculated at constant electrical field. All constants mentioned in the above Eq. (2.7) are represented as matrices with each constant being defined in the x , y and the z direction. Eq. (2.7) relates the mechanical and the electrical parameters of a piezoelectric material. Sirohi and Chopra [17] have discussed the equation formulation for piezoelectric materials. Solving Eq. (2.7) gives us the voltage output commensurate to the mechanical strain generated. Equation (2.7) should not be confused as a (2×2) matrix equation. Here, each quantity is represented as individual matrices. Here, D is a (3×1) matrix and ε is a (6×1) dimensionless matrix. Similarly, E is a (3×1) and σ is a (6×1) matrix. The piezoelectric constants d^d and d^c are defined as (3×6) and (6×3) matrices respectively. The compliance matrix s^E is a (6×6) matrix and the dielectric permittivity is represented as a (3×3) matrix.

2.2 Discretization of Computational Domain

The small energy harvester, which uses piezoelectric patches to generate a voltage due to strain produced, is shown in Figure 2.2. The energy harvester is a T-shaped device consisting of a thin plate with a square tip prism at one end. The plate is fixed at the other end and the square tip mass is free to move. Square patches made of PZT-5A, which is a piezoelectric ceramic made from lead, zirconium and titanium, are attached on either side of the plate near the fixed. These piezoelectric patches are responsible for generating the voltage output from the strain produced in them. Since the harvester body is fixed at one end, it has only one degree of freedom, which is the bending deflection of the beam. The bases of the piezoelectric patches are given zero voltage, and the piezoelectric output is taken from the face opposite to this zero voltage base face.

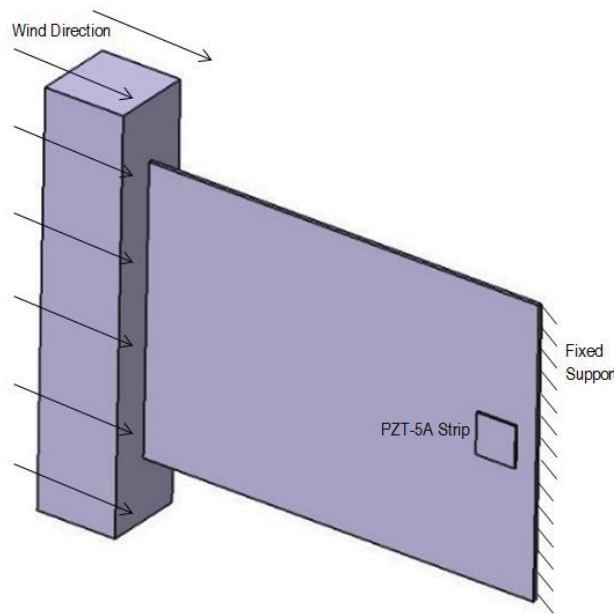


Figure 2.2: Schematic of harvester model

The harvester body is susceptible to aero-elastic instabilities, which are responsible for the generation of voltage across the faces of the piezoelectric patches. The dimensions of the harvester body as in Figure 2.3 are similar to those taken by Kim et al. [18]. However, the only change in the geometry is the use of piezoelectric patches instead of permanent magnets. The dimensions of the plate and the square tip mass are congruent to the harvester dimensions considered by Kim et al. [18]. The piezoelectric patches are taken to be of 0.5 mm thickness.

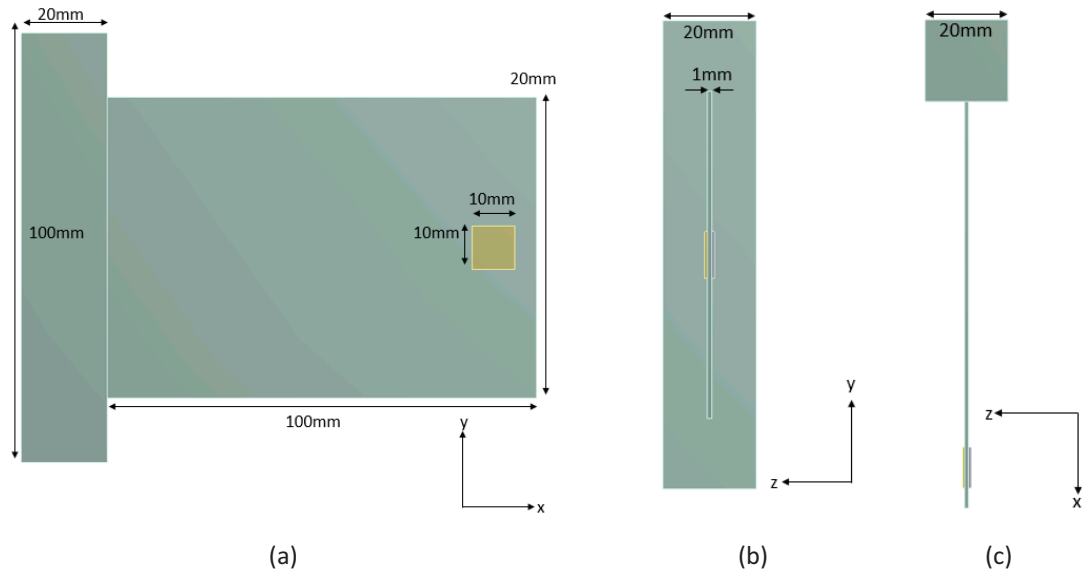


Figure 2.3: Harvester dimensions, (a) Side view, (b) Front View, (c) Top View

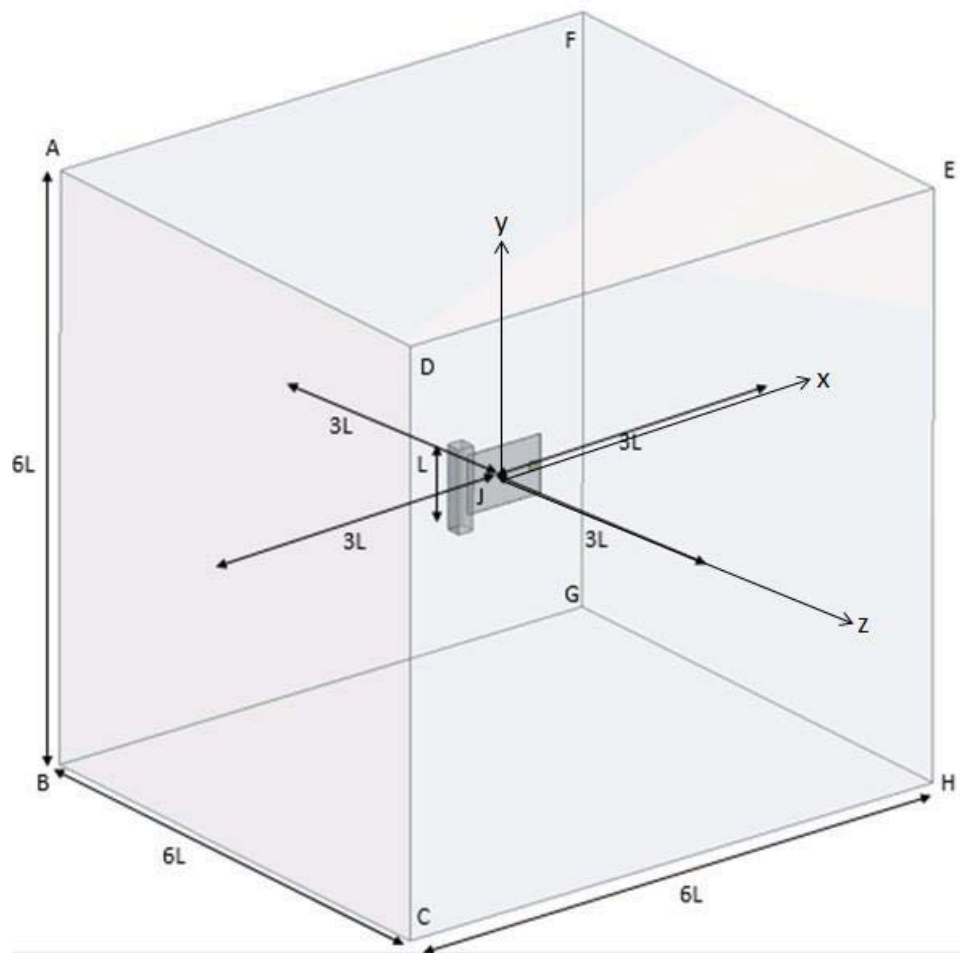


Figure 2.4: Computational domain with boundary conditions

For the computational modeling of the energy harvested subjected to cross wind, a computational domain is created over which the complete simulation takes place. The schematics of the computational domain are shown in Figure 2.4. In Figure 2.4, face ABCD is the inflow, face EFGH is the outflow, and faces ADEF, ABGF, BCHG and DCHE are far-field faces. J represents the harvester position. A three dimensional computational domain consisting of the harvester body of height L is created. The computational domain is a cube of side length $6L$, with the harvester body kept at the center of the cube as shown in Figure 2.4. The inflow boundary condition is kept upstream to the harvester body at a distance of $3L$. The outflow boundary condition is downstream to the harvester body at a distance of $3L$ as well. Thus, the flow of air takes place in the positive x direction. The peripheral walls are at a distance of $3L$ from the harvester body. Velocity at the inflow face is taken as \vec{U} which is taken as a constant for different cases depending on the desired value of the Reynolds number. This velocity is taken as a constant along the x direction for faces ABCD, ADEF, ABGF, BCHG and DCHE. At the outflow face EFGH, the pressure condition corresponding to zero gauge pressure is provided.

Since the harvester is to be kept in free stream, the conditions for the peripheral walls will be similar to that of free stream. Thus, at the peripheral walls, the velocity condition similar to that at the inflow face is provided, i.e., velocity component in the positive x direction as in Eq. (2.8). The structural boundary conditions for the harvester model are set up within the computational modeling. The structural boundary conditions are shown in Figure 2.5.

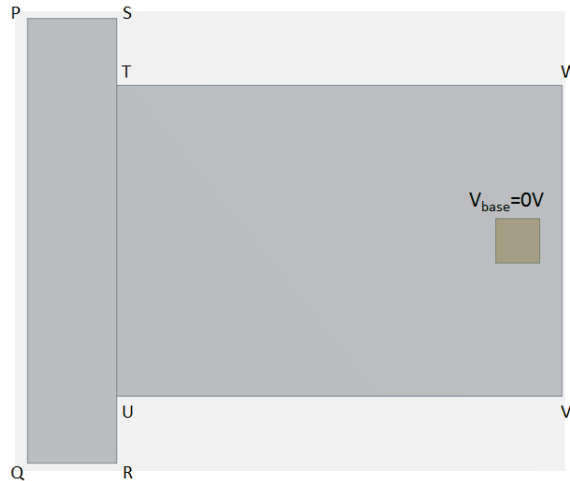


Figure 2.5: Structural boundary conditions

As in Figure 2.5, one end of the harvester model, WV, is fixed whereas the tip mass is free to move. To initiate the flutter of the harvester, an initial pressure is provided to the side of the tip mass to displace it from a certain initial value. The initial deformation provided to the tip mass is 15 mm. The step load is provided to displace the tip mass, after which it is left suddenly to oscillate on its own under the action of the fluid pressure forces.

The piezoelectric coefficients and the material properties for structural steel and PZT-5A are input into the computational modeling. The values of piezoelectric coefficients are taken from the data given by Erturk and Inman [19]. Moreover, for each piezoelectric body, the base voltage is provided as zero volts. The voltage generated due to the strain is measured across the face parallel to the base face. The polarization of the piezoelectric bodies is provided in the z direction. The values for different piezoelectric coefficients used in the modeling, which are used to formulate the matrixes in Eq. (2.7), thus, finding the resulting voltage generated proportional to the strain produced in the piezoelectric bodies, are given in Table 2.1.

Table 2.1: PZT-5A electromechanical and mechanical properties

<i>Property / Coefficient</i>	<i>Value</i>	<i>Property / Coefficient</i>	<i>Value</i>
$s_{11}^E \left(pm^2 N^{-1} \right)$	16.4	d_{33}	374
$s_{12}^E \left(pm^2 N^{-1} \right)$	-5.74	d_{15}	584
$s_{13}^E \left(pm^2 N^{-1} \right)$	-7.22	ep_{11}	1730
$s_{33}^E \left(pm^2 N^{-1} \right)$	18.8	ep_{33}	1700
$s_{55}^E \left(pm^2 N^{-1} \right)$	47.5	Density $\left(kgm^{-3} \right)$	7500
$s_{66}^E \left(pm^2 N^{-1} \right)$	44.3	Young's Modulus (Pa)	6.6×10^{10}
d_{31}	-171	Poisson's Ratio	0.31

The computational domain of interest is tessellated into unstructured tetrahedral cells along the whole fluid domain. Prism layers are generated over the model surface to capture the near wall phenomenon accurately. The total mesh count of the computational domain is 1.05 million. The mesh is refined near the region where the piezoelectric patches are attached to the harvester body in order to capture the deformation of the mentioned section appropriately. This in turn would compute the stress and the strain on each piezoelectric body correctly, thus, giving a correct voltage output for the computational modeling. It is important to keep the skewness for the tetrahedral mesh lower than 0.95 to errors and failure of the mesh during the computational simulation. Thus, for the finite volume mesh generated, the mesh skewness is 0.92. Figure 2.6 shows the structural mesh generated and the mesh generated across the fluid domain for this particular study. The material properties are changed in the structural solver to find the change in the oscillations of the harvester body. Further, for each material in the structural solver, the fluid velocity i.e. the velocity of the air is changed in the computational domain to study the variation in the oscillations and the net voltage output generated.

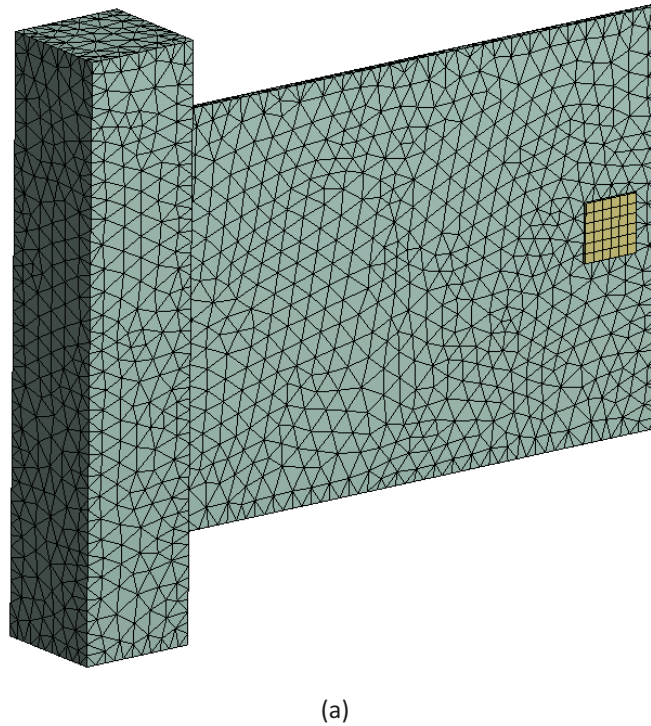


Figure 2.6: Overview of the computational domain, (a) Harvester surface mesh, (b) Surface mesh on thin plate, (c) Mesh structure, (d) Close-up view of mesh showing prism layers (continued)

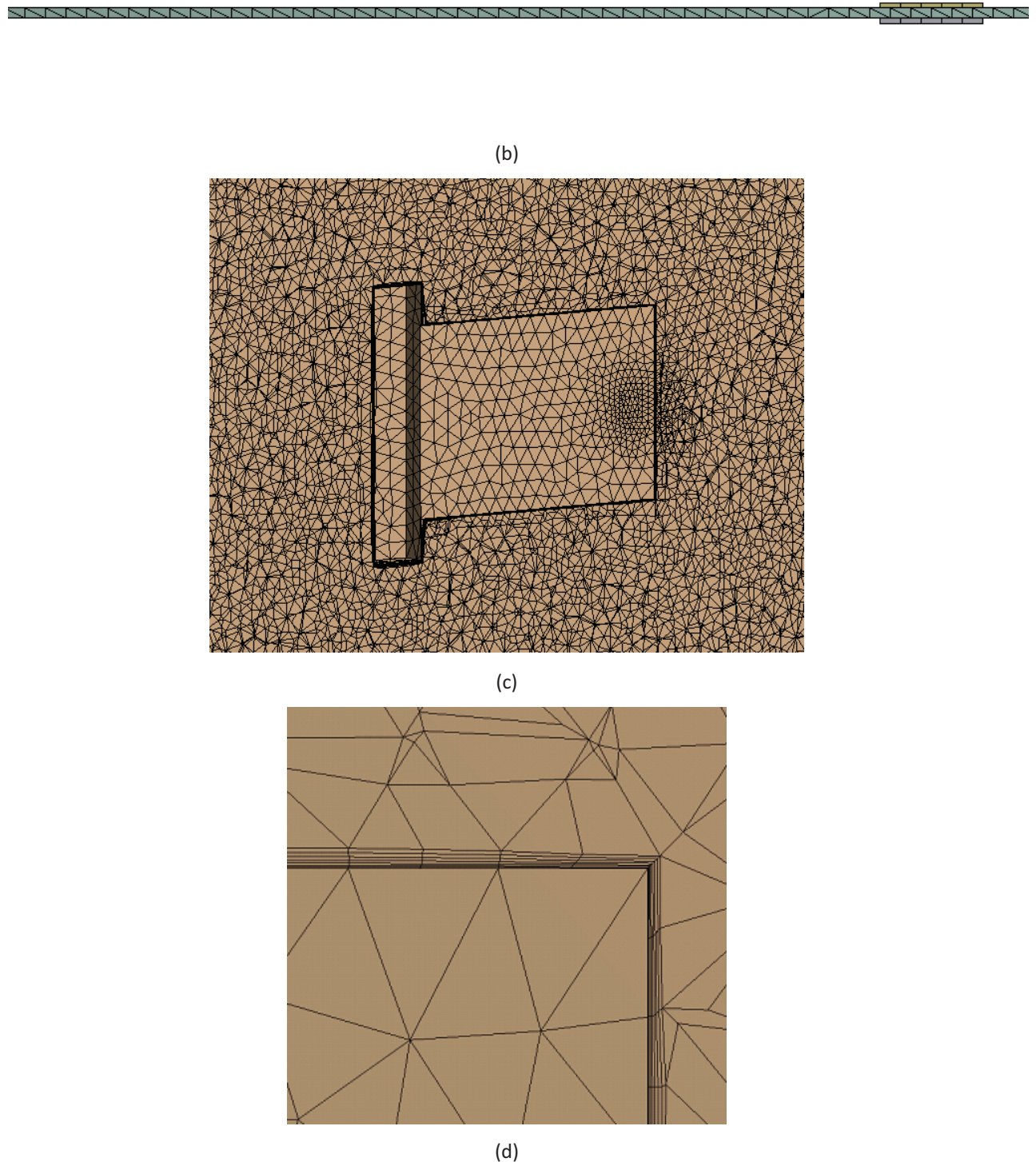


Figure 2.6: Overview of the computational domain, (a) Harvester surface mesh, (b) Surface mesh on thin plate, (c) Mesh structure, (d) Close-up view of mesh showing prism layers

Chapter 3 : Results and Discussions

The current chapter involves the discussion on the computed results of the computational modeling. Section 3.1 involves discussions of the validity of the mesh used to compute the results for this particular study. Further sections present the computed results and the key analysis of the computational study performed on the small energy harvester.

3.1 Spatial Grid Convergence

Computational modeling of tessellated regimes requires a necessary verification of the best possible grid size for the studies performed. This involves the examination of the spatial convergence of the simulation. It is a method to determine the ordered discretization error in a CFD simulation. As we keep refining the grid, the discretization errors should asymptotically approach zero. The approach used to perform the grid convergence study involves generating a fine mesh throughout the domain, then creating coarser meshes by reducing the cell count by a factor of 2, i.e., if the fine mesh has a cell count of 4 million, then one should generate coarser meshes of 2 million and 1 million cells to perform the spatial convergence study as explained by Roache [20]. The order of convergence for the numerical algorithm can be directly obtained from three solutions using a constant mesh refinement ratio and is defined as follows:

$$r = \frac{h_2}{h_1} \quad (3.1)$$

$$C = \frac{\ln\left(\frac{f_3 - f_2}{f_2 - f_1}\right)}{\ln(r)} \quad (3.2)$$

where, r is the constant mesh refinement ratio, h_1 and h_2 are two mesh sizes with h_1 being the finer mesh and h_2 being the coarser mesh, C is the order of convergence, and f_1, f_2 and f_3 are the common computed variables for the three mesh sizes. The exact value or the asymptotic value of any parameter can be obtained by Richardson extrapolation as outlined by Roache [20].

$$P_r = f_1 + \frac{(f_1 - f_2)}{r^C - 1} \quad (3.3)$$

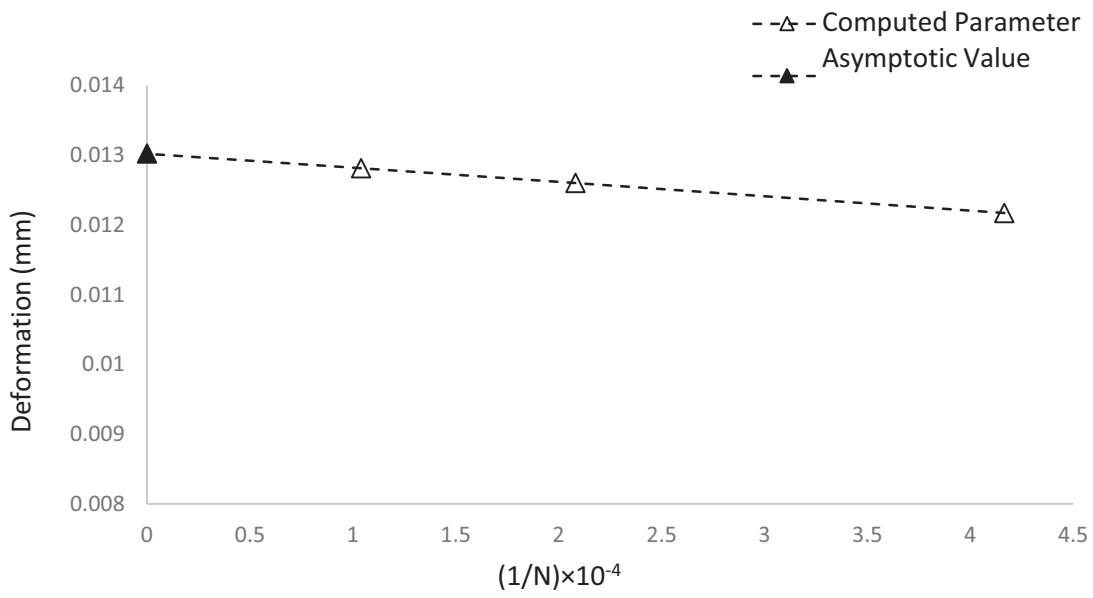
where, P_r represents the asymptotic value or the exact value of the parameter being monitored. The Grid Convergence Index as outlined by Roache [20] is as follows:

$$GCI_{fine} = \frac{F_s |\varepsilon|}{r^C - 1} \quad (3.4)$$

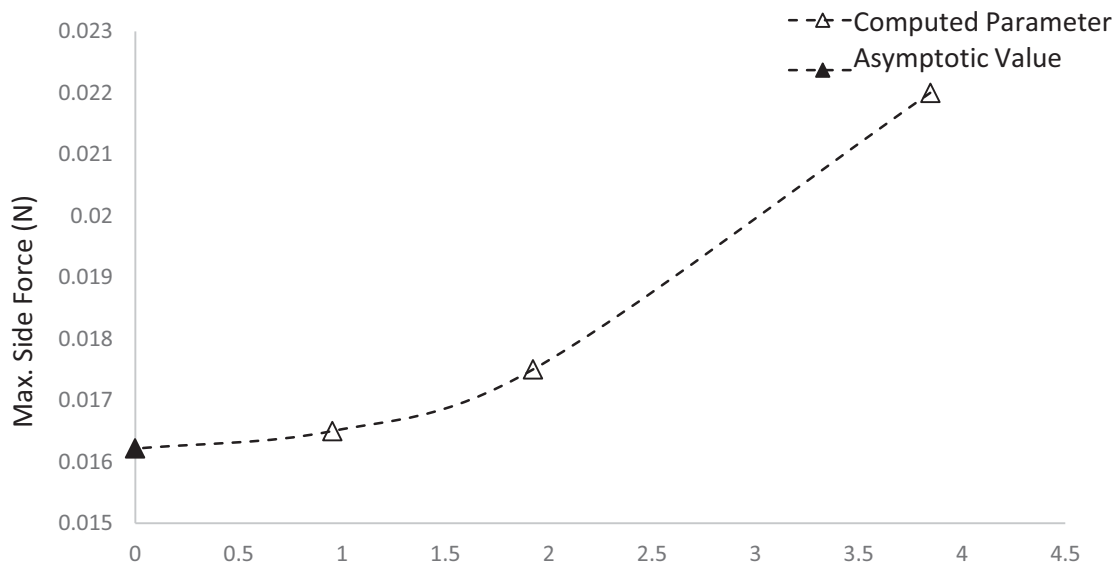
$$\varepsilon = \frac{f_2 - f_1}{f_1} \quad (3.5)$$

where, F_s is the factor of safety and ε is the relative error of two successive meshes. For cases where only two meshes are considered, the value of factor of safety is taken as 3. However, for cases where three or more meshes are being compared, the value of factor of safety is taken as 1.25. For the calculations of the grid convergence, the value of factor of safety is taken as 1.25 here.

The grid convergence study is performed for both the finite volume fluid mesh and the finite element structural mesh. The mesh count for the structural mesh comes out to be around 9600 cells and that for the fluid domain comes out to be around 1.05 million cells as shown in section 2.2. For the grid convergence study of the fluid domain, the maximum side force on one complete side of the energy harvester is monitored for different mesh counts. Similarly, for the grid convergence of the structural mesh, the deformation of the harvester corresponding to a fixed applied side force, which is computed from the steady fluid analysis, is monitored for different mesh counts as shown in Figure 3.1. The GCI for the fluid domain is 2.16% and that for the structural mesh is 2.03%. Figure 3.1 shows the graphs for the grid convergence study performed for both the structural and the fluid domain meshes. As can be seen from Figure 3.1, the computational mesh used for both the structural and the fluid analysis is very close to the asymptotic value. Hence, results computed using the above mentioned mesh counts are very close to the actual result values.



(a)



(b)

Figure 3.1: Spatial grid convergence, (a) Tip deformation variation for structural mesh, (b) Side force variation for fluid mesh

3.2 Computed Flow Past the Energy Harvester for Reynolds Number Equal to 0.89×10^5

For the boundary conditions explained and mentioned in section 2.2, the flow past the small energy harvester is computed for the given wind speed. The pressure contours, velocity contours and the wall shear stress at different instances of time are presented for two different cases, where the harvester body material is changed. The two cases presented are of the harvester body made of aluminium and structural steel. The dimensions and boundary conditions are kept the same for both cases. The flow field is computed for a speed of 9m/s where the Reynolds number is calculated to be 0.89×10^5 , which is well in the laminar range for external flow.

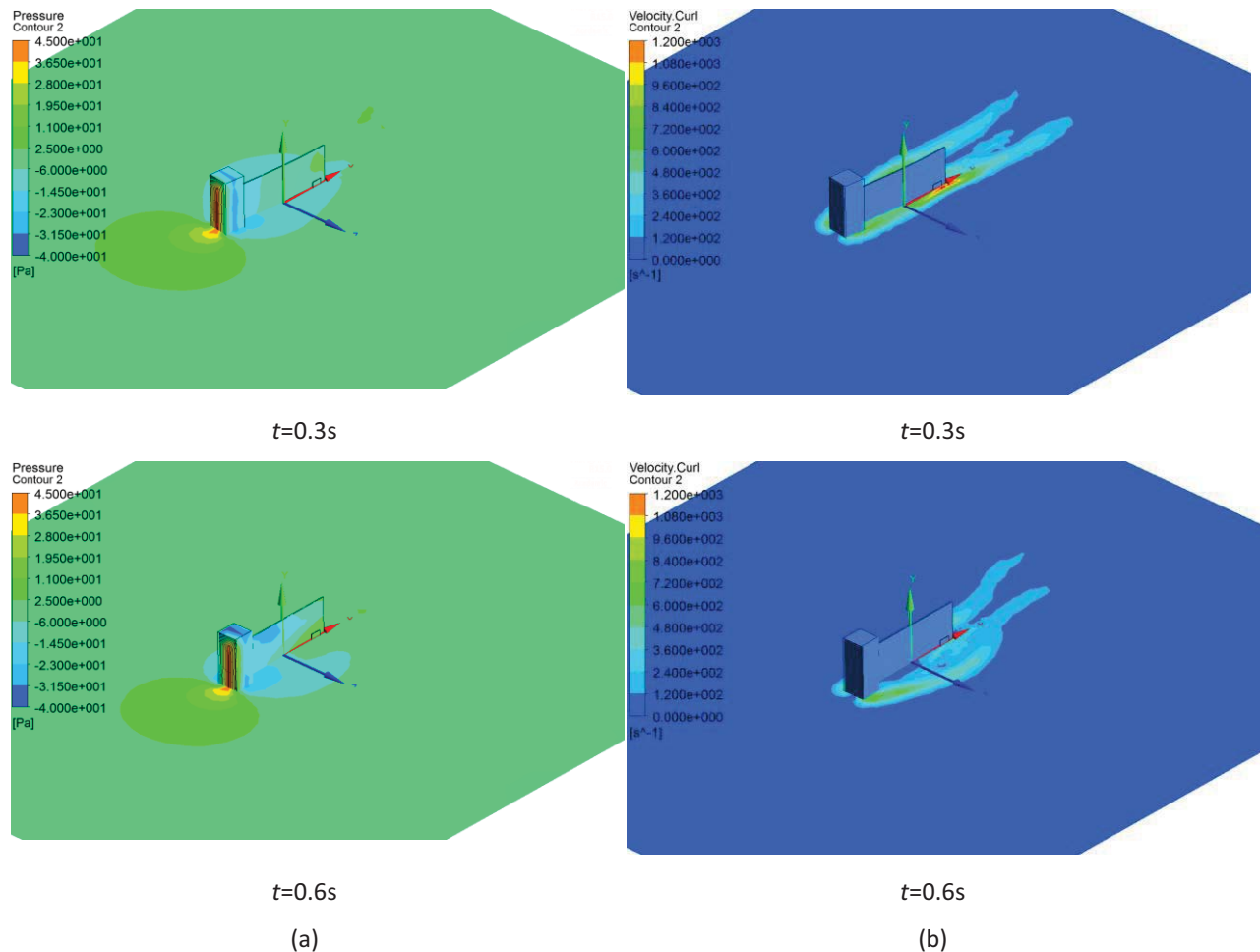


Figure 3.2: (a) Pressure and (b) Vorticity contours for aluminium harvester at specified time instants t for wind speed of 9m/s (continued)

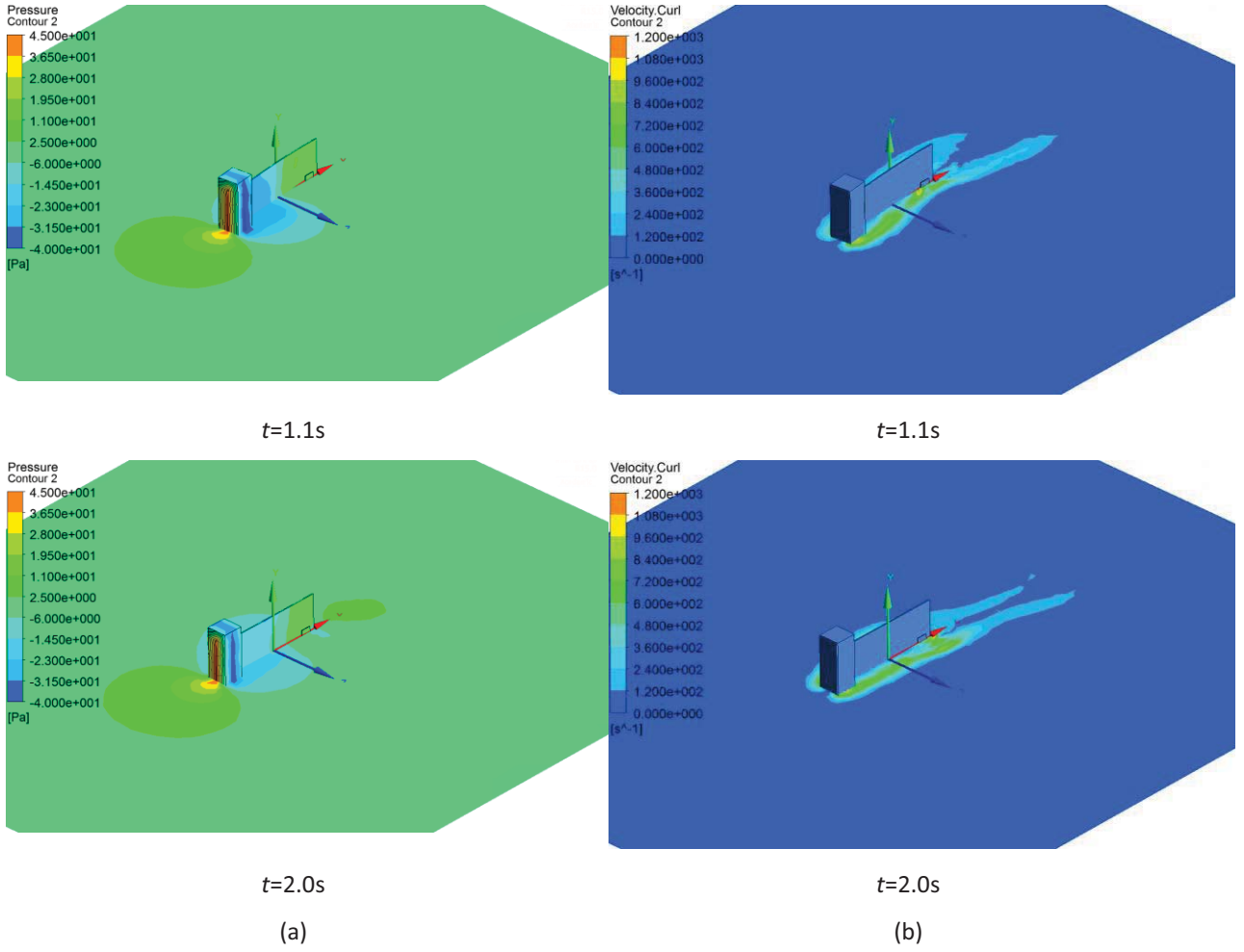


Figure 3.2: (a) Pressure and (b) Vorticity contours for aluminium harvester at specified time instants t for wind speed of 9m/s

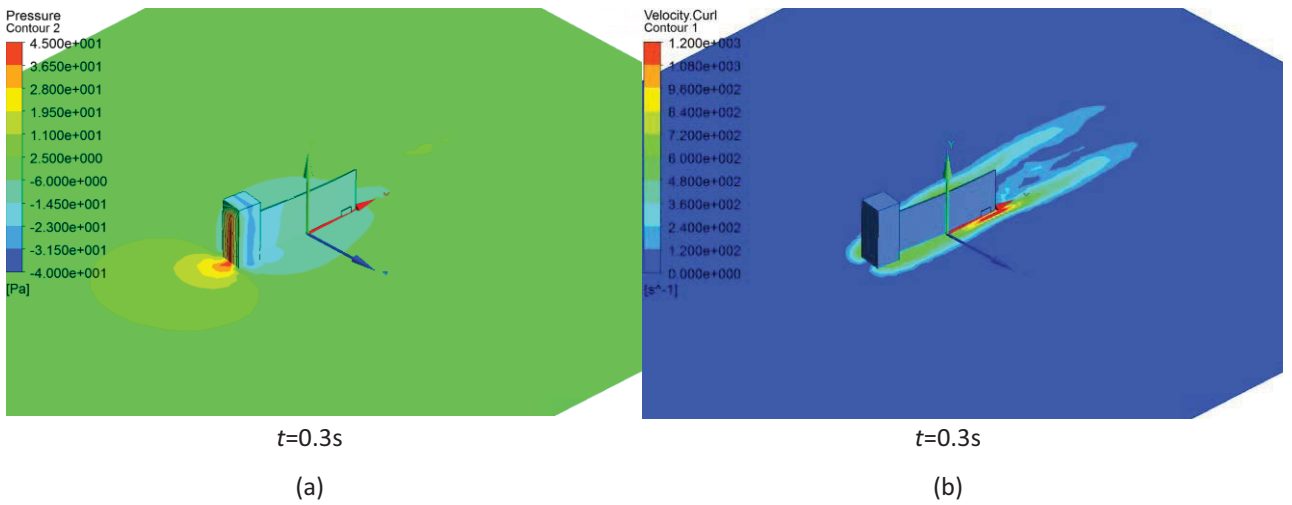


Figure 3.3: (a) Pressure and (b) Vorticity contours for structural steel harvester at specified time instants t for wind speed of 9m/s (continued)

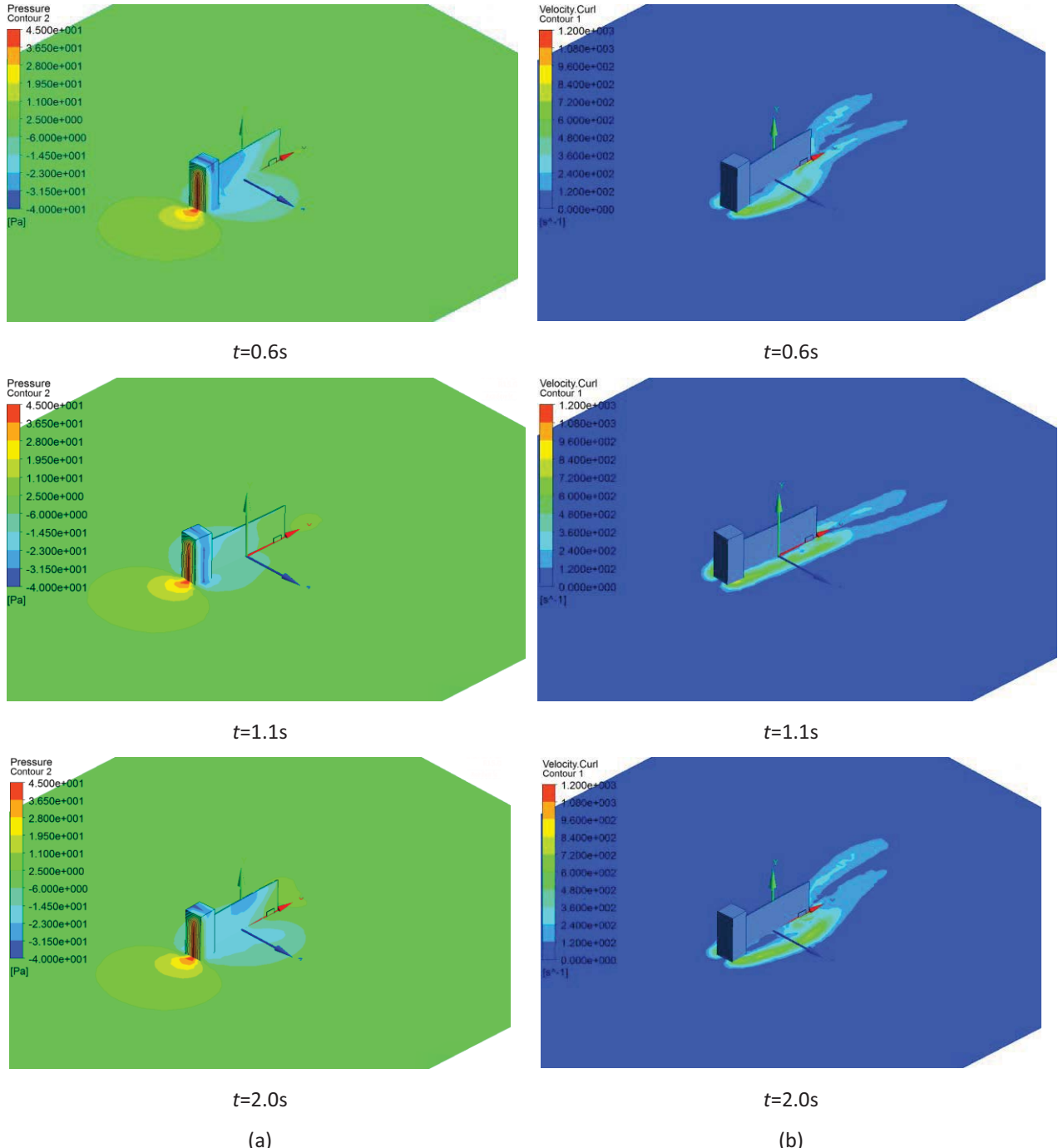


Figure 3.3: (a) Pressure and (b) Vorticity contours for structural steel harvester at specified time instants t for wind speed of 9m/s

Figures 3.2 and 3.3 show the variation of pressure and vorticity through different instances of the flow past the small energy harvester for the aluminium and structural steel materials. As can be clearly seen, the pressure contours for both materials is nearly the same up until 0.3s. This is because at 0.3s, both the material harvesters are provided with the same initial displacement of 15mm. After the harvester has been left and the force is removed, it is free to oscillate about its own. Thus, a clear variation in the pressure contours can be seen at the subsequent times. Due to the material properties, the nature of oscillation of the aluminium and the structural steel harvester differs. As a result, the pressure contour at the same time instance will be different for both cases. From Figures 3.2 and 3.3, at $t=1.1s$, the aluminium harvester is at one extreme position while the structural steel harvester is at the other extreme. Thus, material properties will contribute to the nature of oscillations. The animations for the pressure, vorticity and velocity contours for this case are uploaded on a Youtube channel, the links of which are [Pressure-Al-9m/s](#), [Vorticity-Al-9m/s](#) and [Velocity-Al-9m/s](#) for the aluminium harvester and [Pressure-SS-9m/s](#), [Vorticity-SS-9m/s](#), and [Velocity-SS-9m/s](#) for the structural steel harvester.

Similar to the pressure contours, the vorticity contours for the aluminium and the structural steel harvesters are nearly the same up until 0.3s due to the same displacement of the tip mass in both cases. However, once both harvesters are left to oscillate on their own due to interaction with the wind flow around it, there is a noticeable variation in the vortices generated at different time instances as is evident from Figures 3.2 and 3.3. Further, one can notice the difference in the wakes in both cases. Due to the difference in the material properties, both harvesters oscillate differently. As a result, at the same time instance, the wakes formed will be different for both material harvesters. The wall shear acting on the surface of the harvester only determines the interaction of the fluid on the solid. If the material geometry is kept the same and if we do not account for the surface roughness for the different materials, the wall shear acting on the harvester will be the same irrespective of the material being chosen. However, Figure 3.4 shows the variation in the wall shear. The variation is simply due to the nature of the oscillations and material properties.

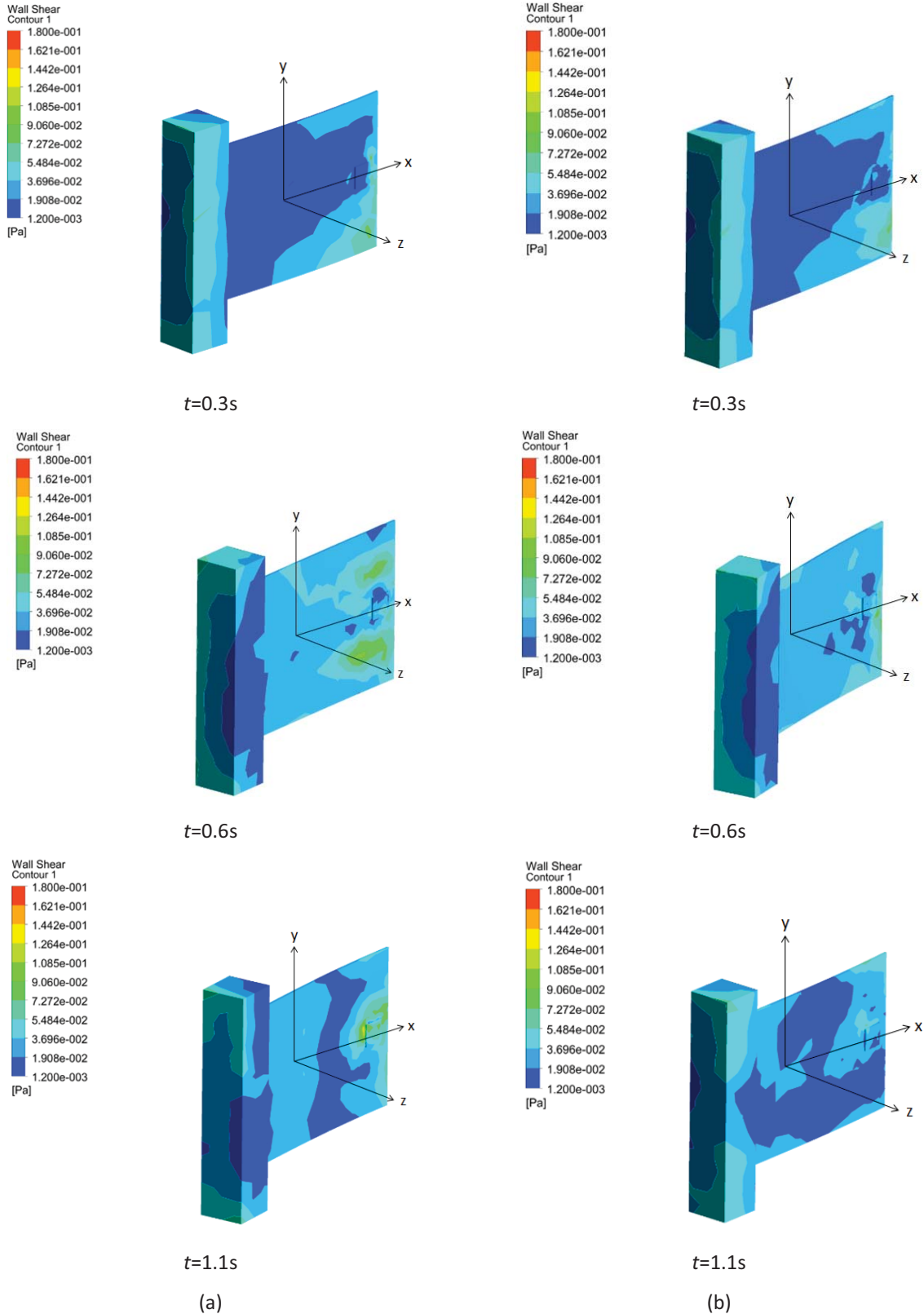


Figure 3.4: (a) Aluminium and (b) Structural Steel wall shear contours at specified time instants t for wind speed of 9m/s (continued)

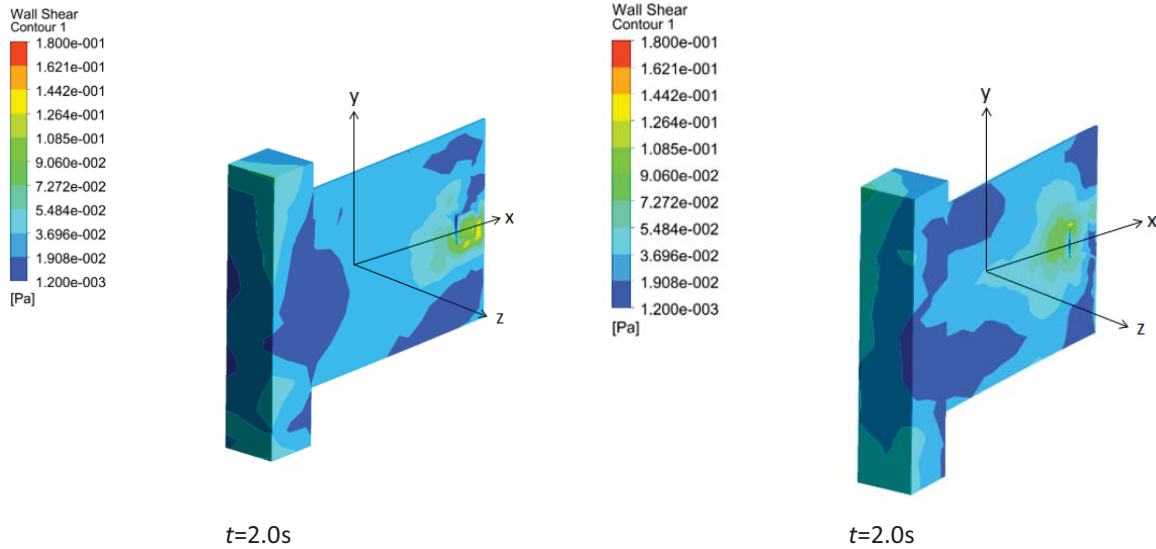
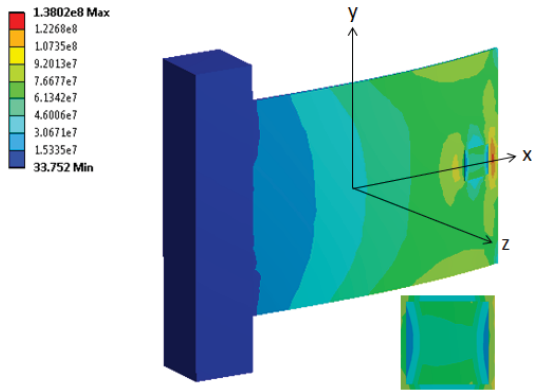


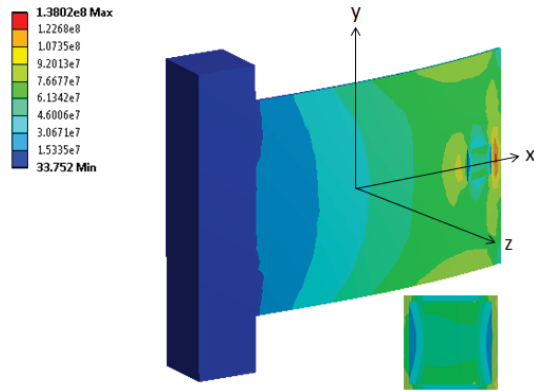
Figure 3.4: (a) Aluminium and (b) Structural Steel wall shear contours at specified time instants t for wind speed of 9m/s

As seen from Figure 3.4, at time 0.3s, the wall shear is nearly the same for both harvesters which suggests that the wall shear is not dependent on the material chosen. However, if the surface roughness is taken into consideration, the wall shear may differ. The pressure field, the vortices generated and the wall shear for both harvesters is different at different time instances. However, these values are different simply due to the material property of the harvester. The material property defines the nature of flutter of the harvester. The harvester made of the material with a lower Young's modulus is likely to flutter more than the one with a higher Young's modulus as is the case here. The flow field is, thus, dependent on the structural properties of the solid. The animation links for the same are [Stress-Al-9m/s](#) and [Stress-SS-9m/s](#).

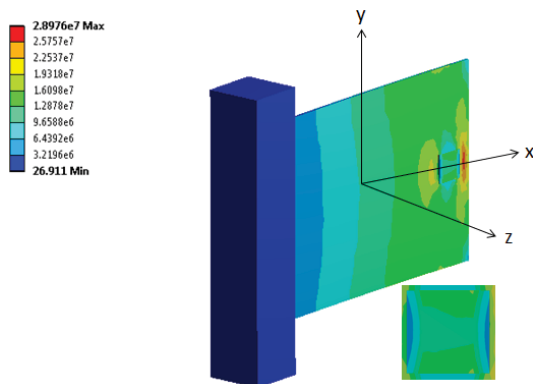
The results from the structural analysis are incorporated in this study. The comparison between the nature of oscillation for the aluminium harvester and the structural steel harvester is presented. The stress generated in the harvesters is shown in Figure 3.5 for different instances of time. The variation in the tip mass displacement for both harvester cases is shown in Figure 3.6(a). Since the piezoelectric voltage generated by each piezo body is dependent on the strain, the maximum strain for both harvesters is compared and is shown in Figure 3.6(b). Consequently, the piezo electric voltage generated by both piezo bodies is compared for both material harvesters and is presented in Figure 3.6(c) and 3.6(d).



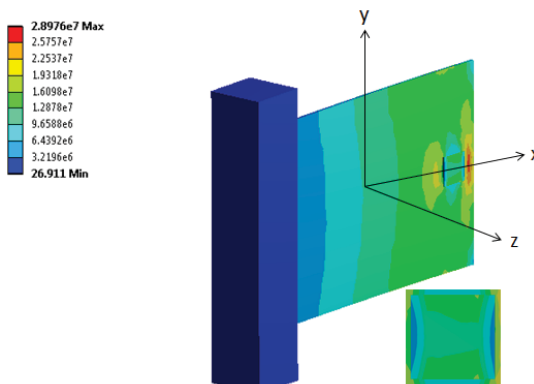
$t = 0.3\text{s}$



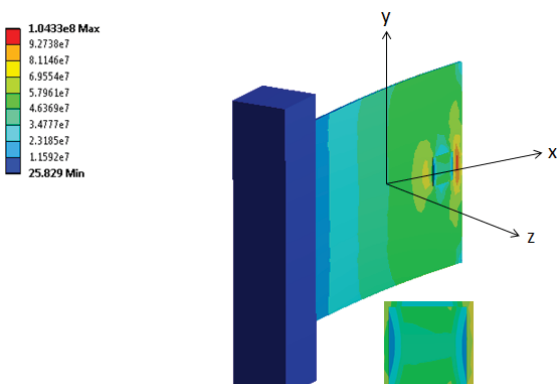
$t = 0.3\text{s}$



$t = 0.6\text{s}$

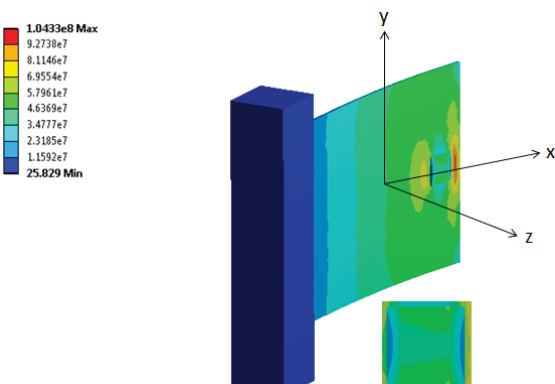


$t = 0.6\text{s}$



$t = 1.1\text{s}$

(a)



$t = 1.1\text{s}$

(b)

Figure 3.5: (a) Aluminium and (b) Structural Steel von Mises stress contours at specified time instants t for wind speed of 9m/s (inset, stress on piezoelectric strip) (continued)

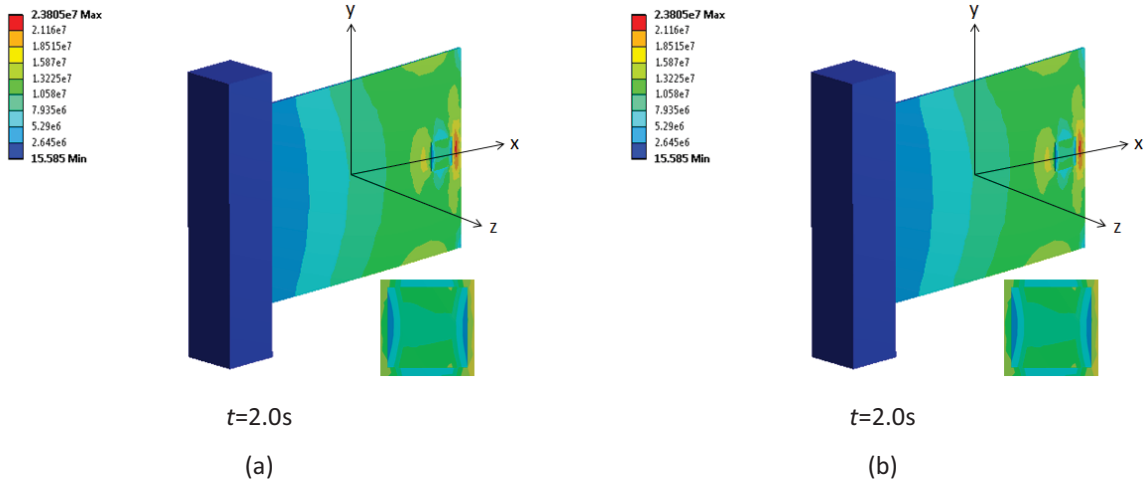


Figure 3.5: (a) Aluminium and (b) Structural Steel von Mises stress contours at specified time instants t for wind speed of 9m/s (inset, stress on piezoelectric strip)

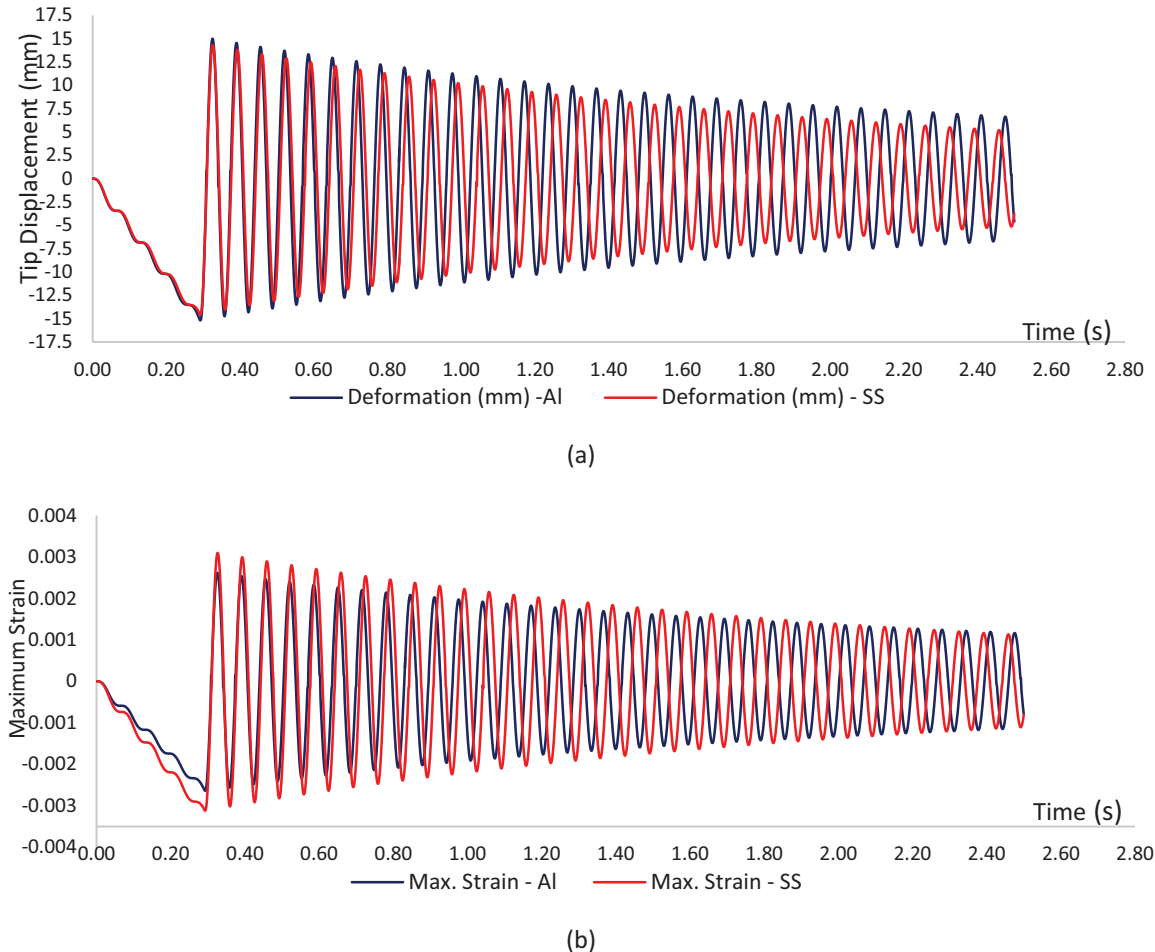
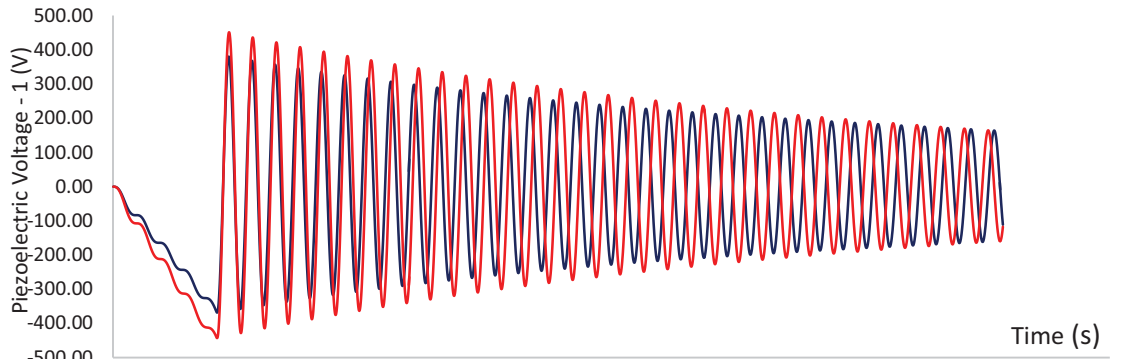
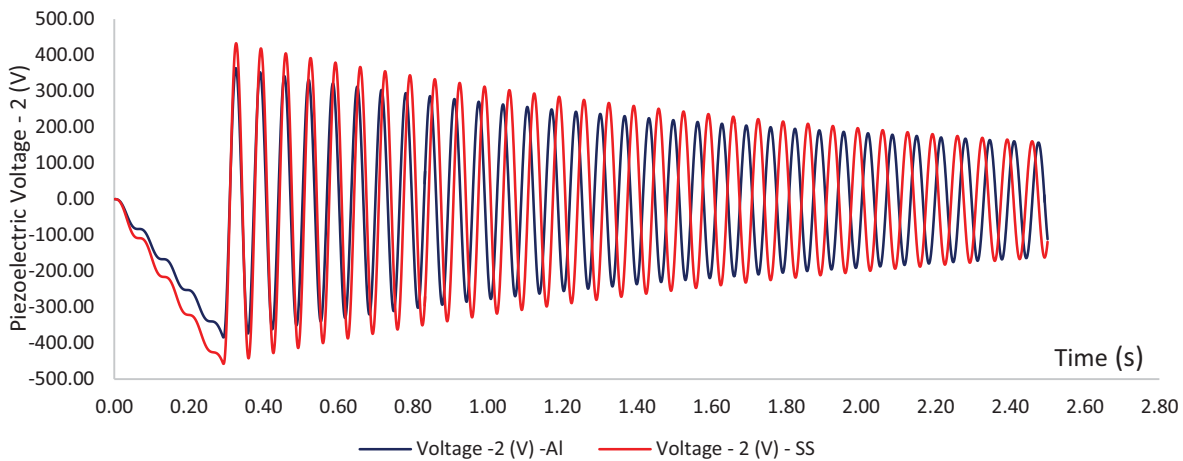


Figure 3.6: Variation of parameters for different materials at 9m/s, (a) Tip displacement, (b) Maximum strain, (c) Piezoelectric voltage from piezo body-1, (d) Piezoelectric voltage from piezo body-2 (continued)



(c)



(d)

Figure 3.6: Variation of parameters for different materials at 9m/s, (a) Tip displacement, (b) Maximum strain, (c) Piezoelectric voltage from piezo body-1, (d) Piezoelectric voltage from piezo body-2

As is evident from Figure 3.6, the damping of the oscillation motion is greater in case of the structural steel harvester than that of the aluminium harvester. This is due to the greater strength of structural steel when compared to aluminium. The Young's modulus for structural steel is about 2×10^{11} whereas that for aluminium is 7.1×10^{10} . This difference in the material property of the harvester is what controls the nature of oscillations over the simulated time. From Figure 3.9(a), it can be seen that the aluminium harvester will completely damp out its oscillatory motion at a time greater than the structural steel harvester. Thus, the aluminium harvester will give a voltage output from the piezoelectric bodies for a greater duration than the structural steel harvester and thus, is more favorable while designing the harvester.

For a laminar wind velocity, the computational modeling of the flow around the small energy harvester suggests that the aluminium is a preferable material than structural steel while designing the harvester. However, the computational modeling for higher wind speeds needs to be carried out in order to study the efficacy of this harvester, such that it does not succumb to the aero-elastic instabilities and fail while operating on higher wind speeds. Section 3.3 discusses the computational model for the same.

3.3 Computed Flow Past the Energy Harvester for Reynolds Number Equal to 2.28×10^5

For the boundary conditions explained and mentioned in section 2.2, the flow past the small energy harvester is computed for the given wind speed. The pressure contours, velocity contours and the wall shear stress at different instances of time are presented for two different cases, where the harvester body material is changed. The two cases presented are of the harvester body made of aluminium and structural steel. The dimensions and boundary conditions are kept the same for both cases. The flow field is computed for a speed of 23m/s where the Reynolds number is calculated to be 2.28×10^5 , which is well in the laminar range for external flow.

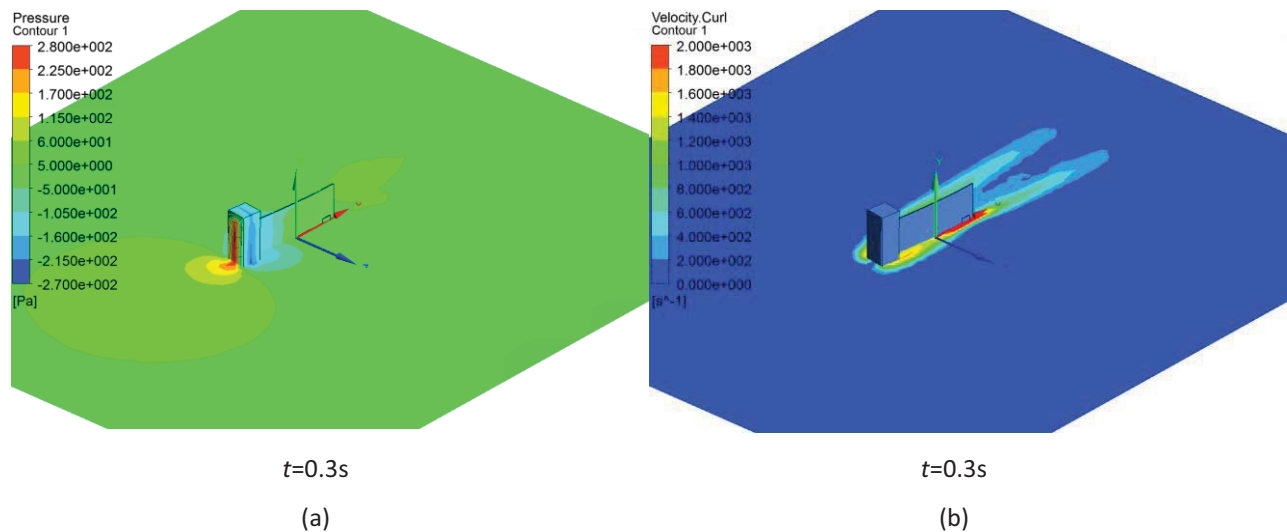


Figure 3.7: (a) Pressure and (b) Vorticity contours for aluminium harvester at specified time instants t for wind speed of 23m/s (continued)

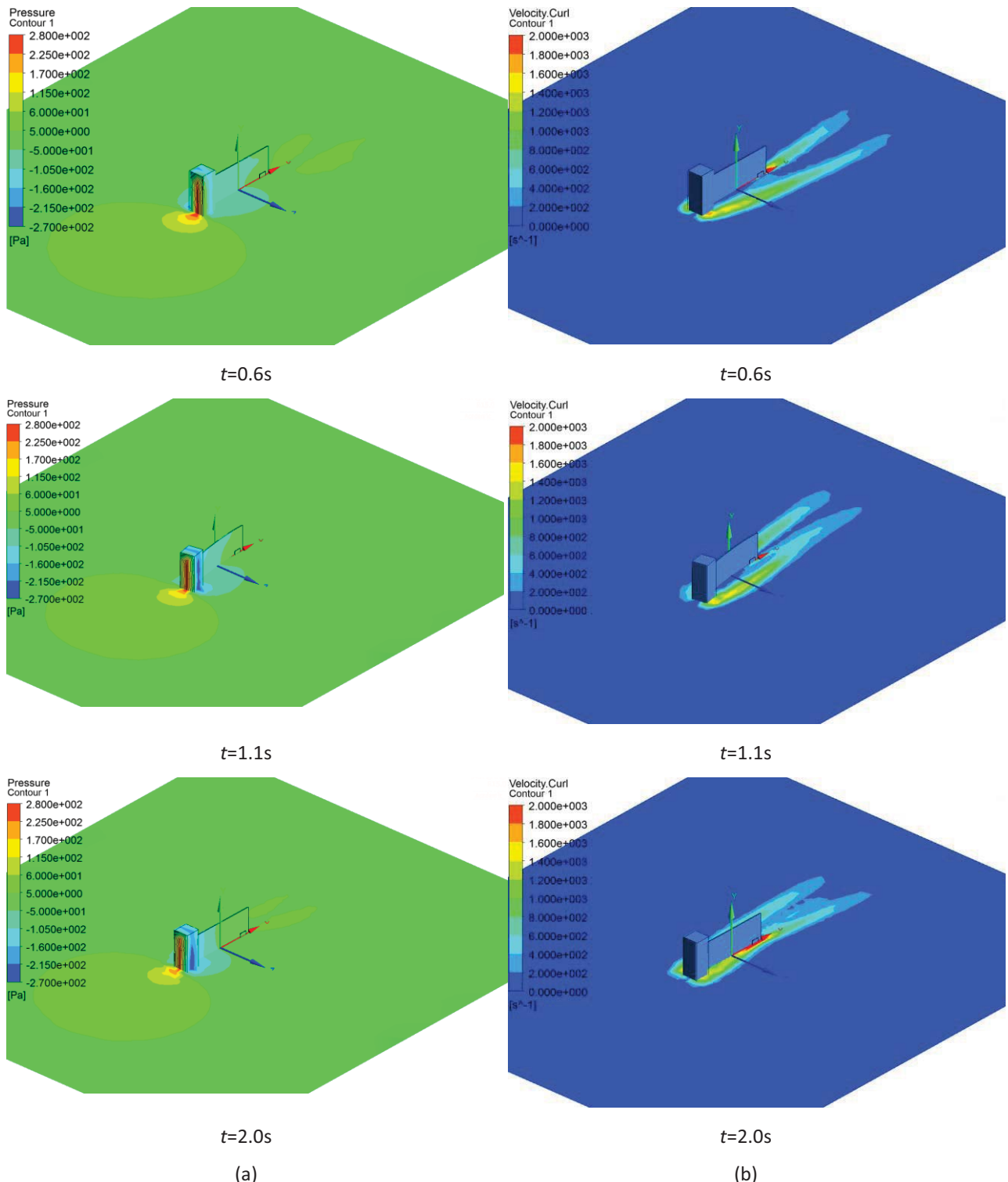


Figure 3.7: (a) Pressure and (b) Vorticity contours for aluminium harvester at specified time instants t for wind speed of 23m/s

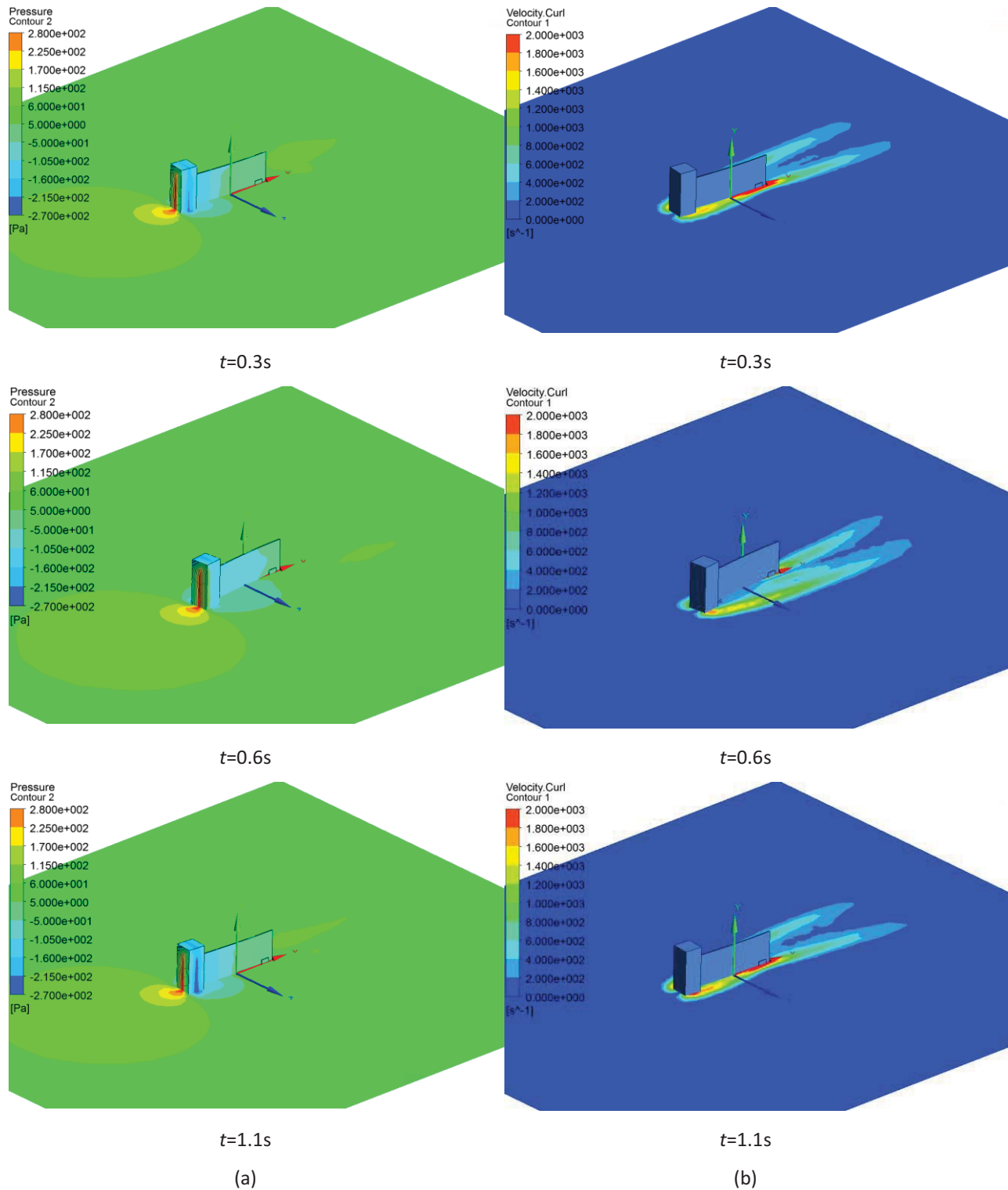


Figure 3.8: (a) Pressure and (b) Vorticity contours for structural steel harvester at specified time instants t for wind speed of 23m/s (continued)

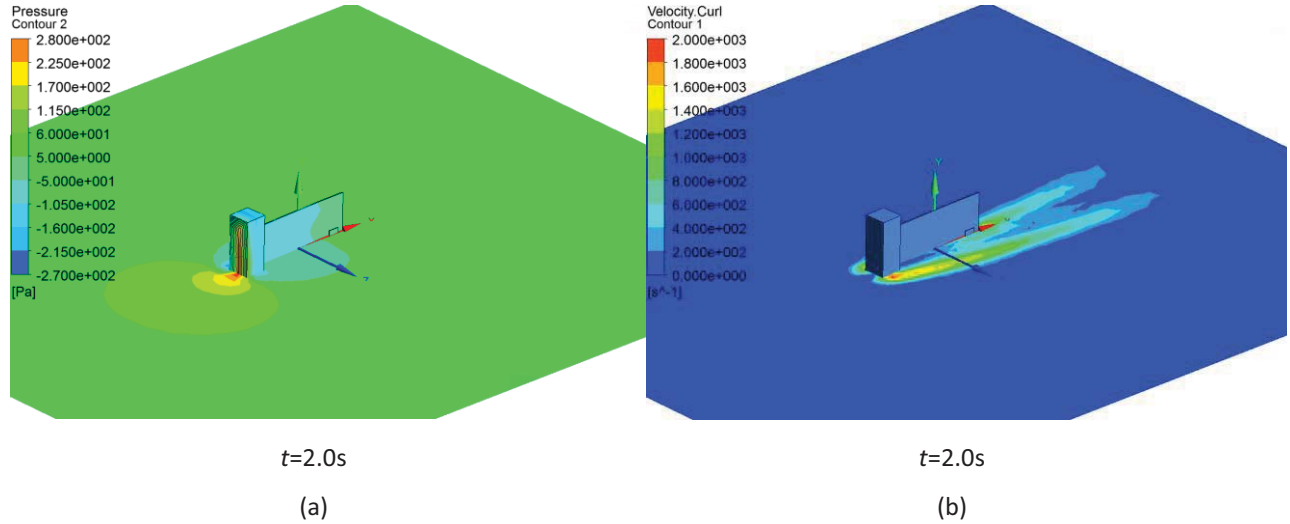


Figure 3.8: (a) Pressure and (b) Vorticity contours for structural steel harvester at specified time instants t for wind speed of 23m/s

Figures 3.7 and 3.8 show the variation in the pressure field and the vorticity for a wind speed of 23m/s for the aluminium and the structural steel harvester. The contours at time 0.3s simply show that at the initial displacement for both harvesters, the flow field is exactly the same for the same dimensions. After the harvesters are left to oscillate on their own, the contours change over time as is evident from Figure 3.7 and 3.8. As explained in section 3.2, the difference in the contour plots is due to the structural properties of the harvesters. The difference in the Young's modulus is what affects the nature of oscillation in the flow field. A significant difference from the laminar case can be seen in the turbulent case. The range of pressure acting throughout the simulation time is greater than the laminar case. Thus, the harvester experiences a greater instability due to the fluid flow as compared to the laminar case. The nature of flutter oscillation should thus, be greater in case of the turbulent wind speed with respect to the laminar wind speed. The animations showing the pressure, the vorticity and the velocity contours are uploaded to a Youtube channel, the links of which are [Pressure-Al-23m/s](#), [Vorticity-Al-23m/s](#) and [Velocity-Al-23m/s](#) for the aluminium harvester and [Pressure-SS-23m/s](#), [Vorticity-SS-23m/s](#) and [Velocity-SS-23m/s](#) for the structural steel harvester.

The wall shear contours for each harvester case is shown in Figure 3.9.

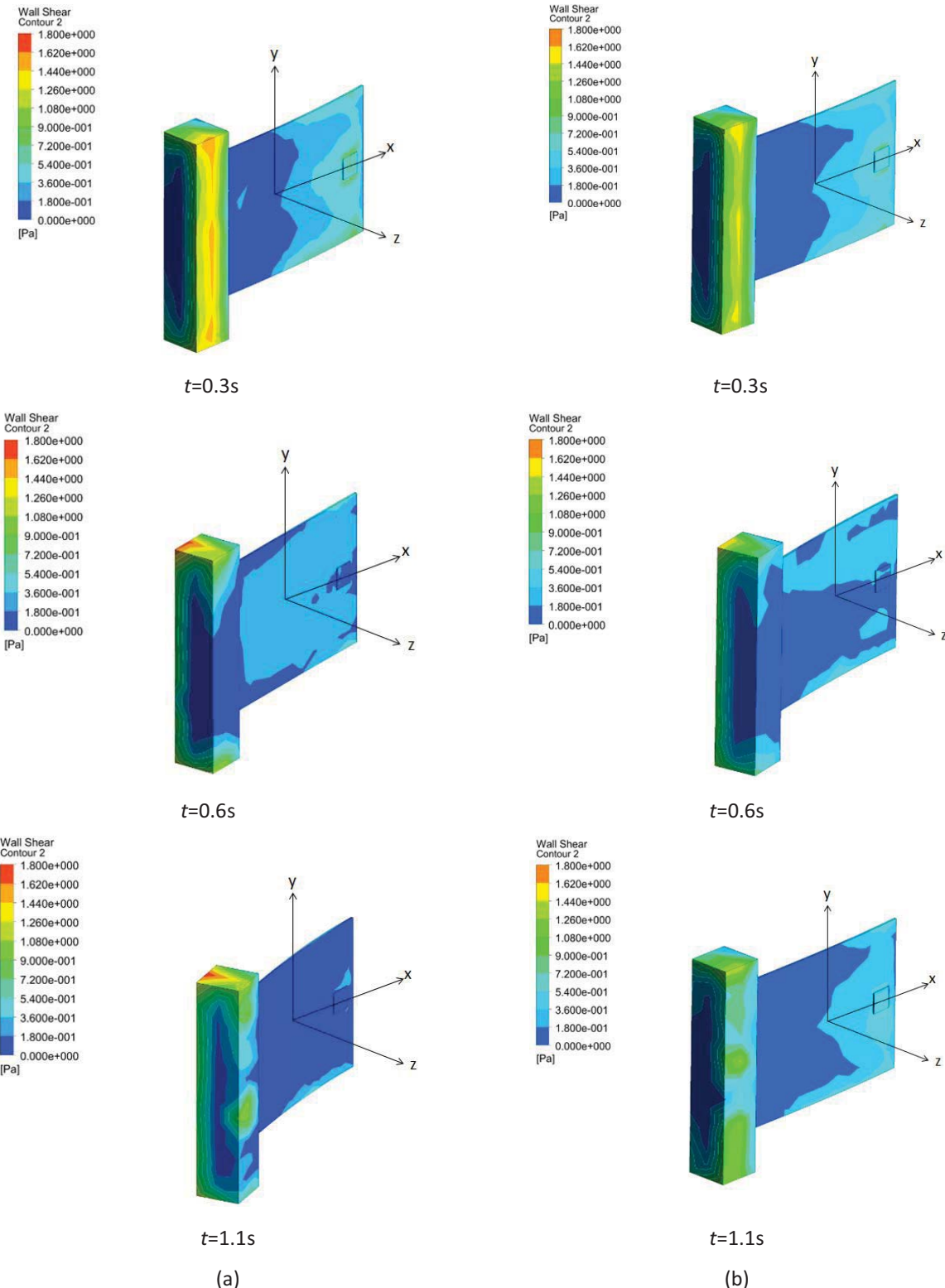


Figure 3.9: (a) Aluminium and (b) Structural Steel wall shear contours at specified time instants t for wind speed of 23m/s (continued)

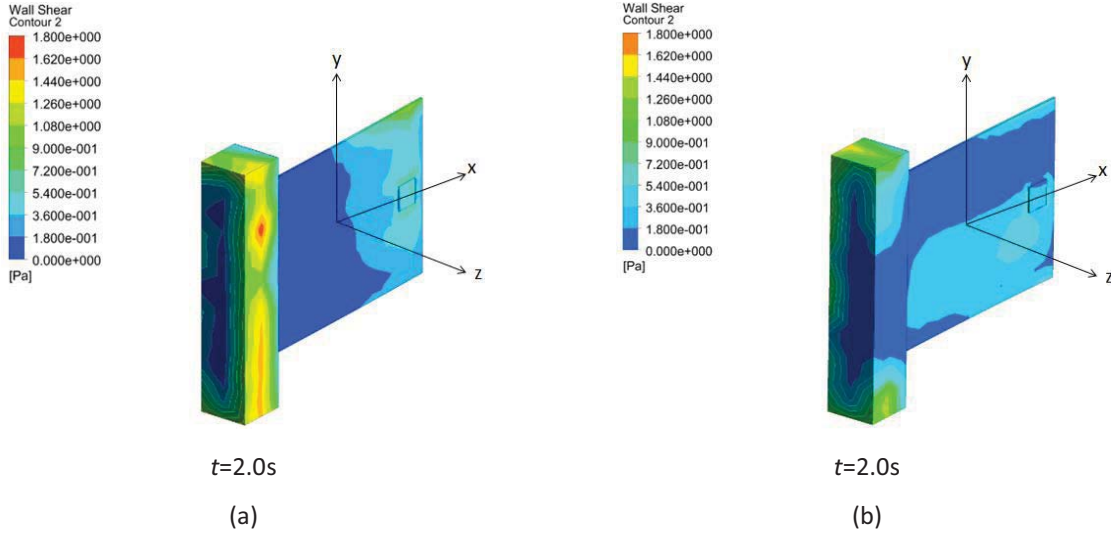


Figure 3.9: (a) Aluminium and (b) Structural Steel wall shear contours at specified time instants t for wind speed of 23m/s

As can be seen from Figure 3.9, the wall shear contour at 0.3s is nearly the same for both harvesters suggesting that the wall shear does not depend on the harvester material. However, the supposition taken here does not account for surface roughness of the harvesters. Furthermore, the magnitude of the wall shear is greater for the turbulent wind speed than that of the laminar wind speed. Again, the variation at different time steps is due to the structural properties and the variation in the oscillation nature. The wall shear will be same for both the harvesters for the same position considering that the surface roughness is not given due consideration. Figure 3.10 and 3.11 show the variation of stress and the structural parameters computed during the computational modeling respectively.

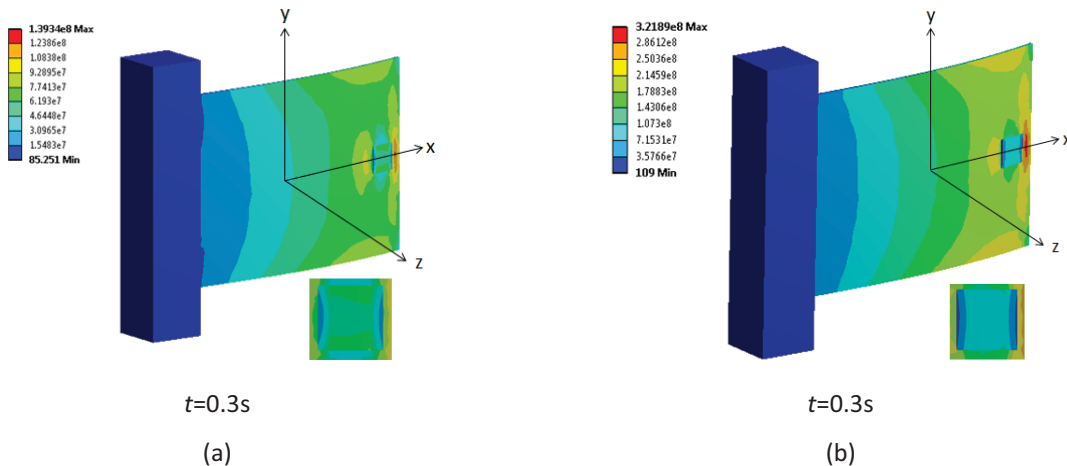


Figure 3.10: (a) Aluminium and (b) Structural Steel von Mises stress contours at specified time instants t for wind speed of 23m/s (inset, stress on piezoelectric strip) (continued)

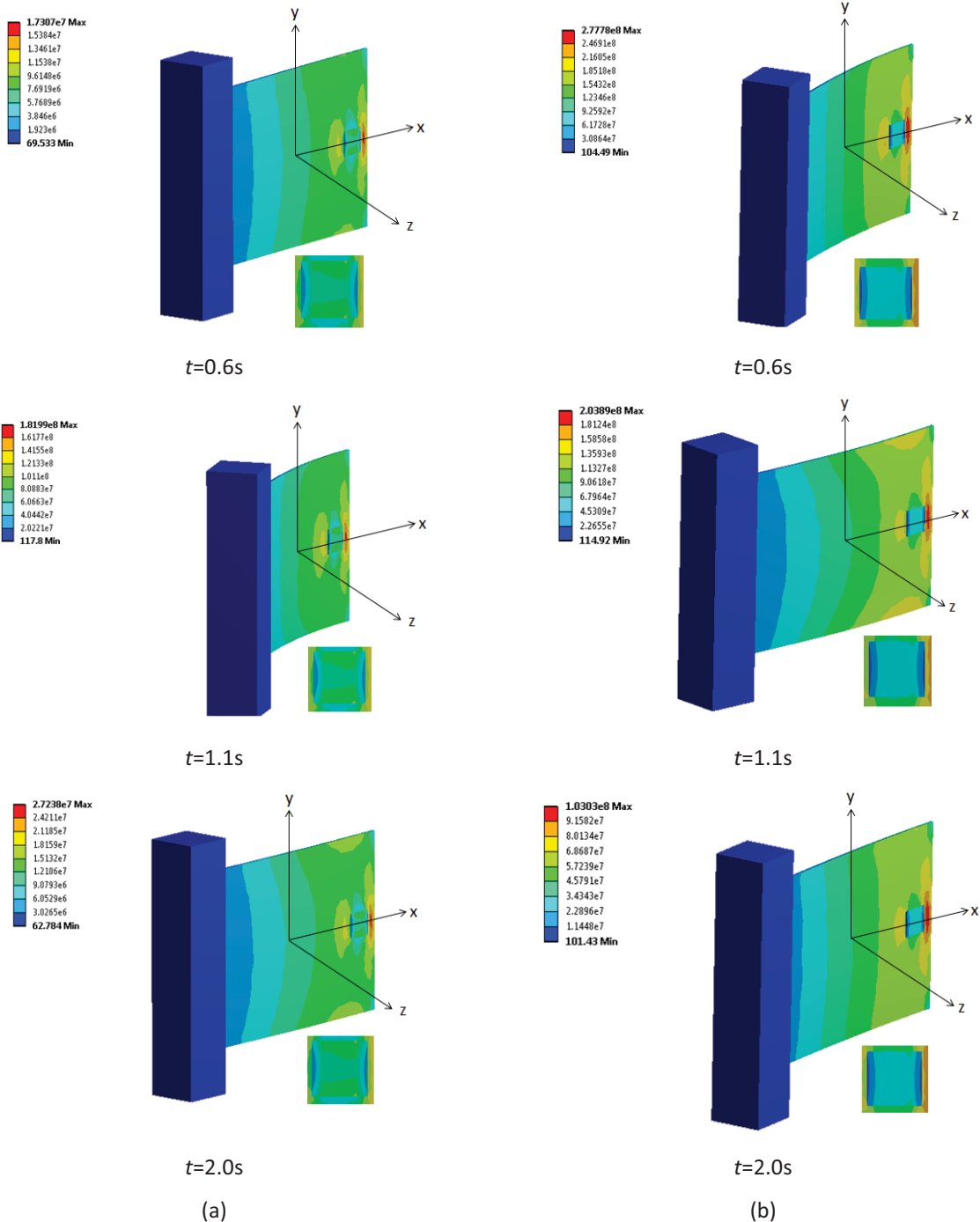
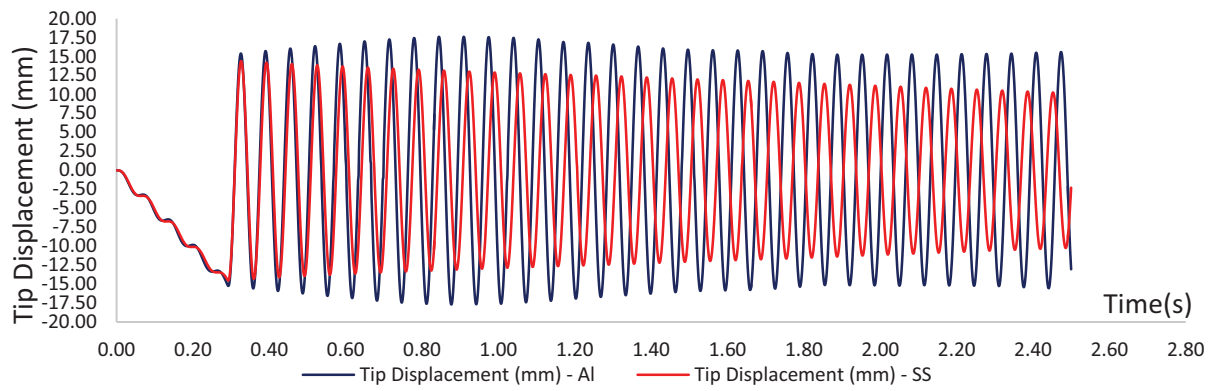
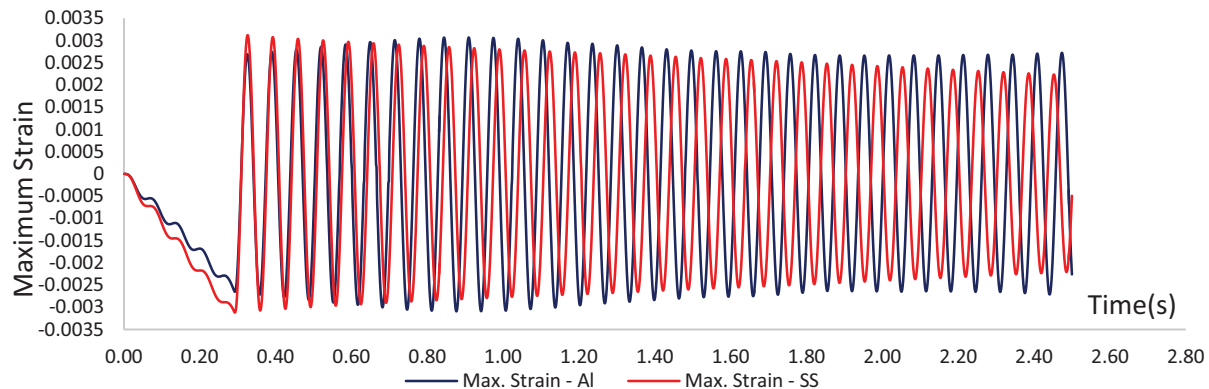


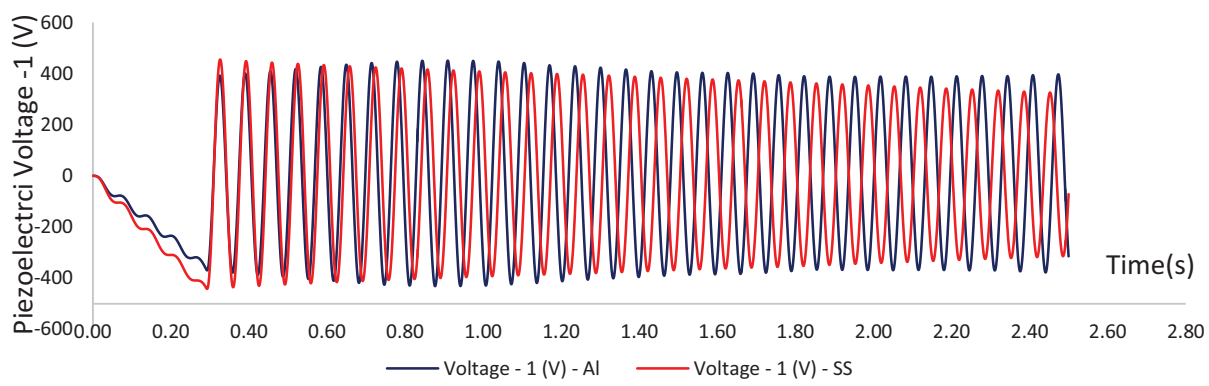
Figure 3.10: (a) Aluminium and (b) Structural Steel von Mises stress contours at specified time instants t for wind speed of 23m/s (inset, stress on piezoelectric strip)



(a)

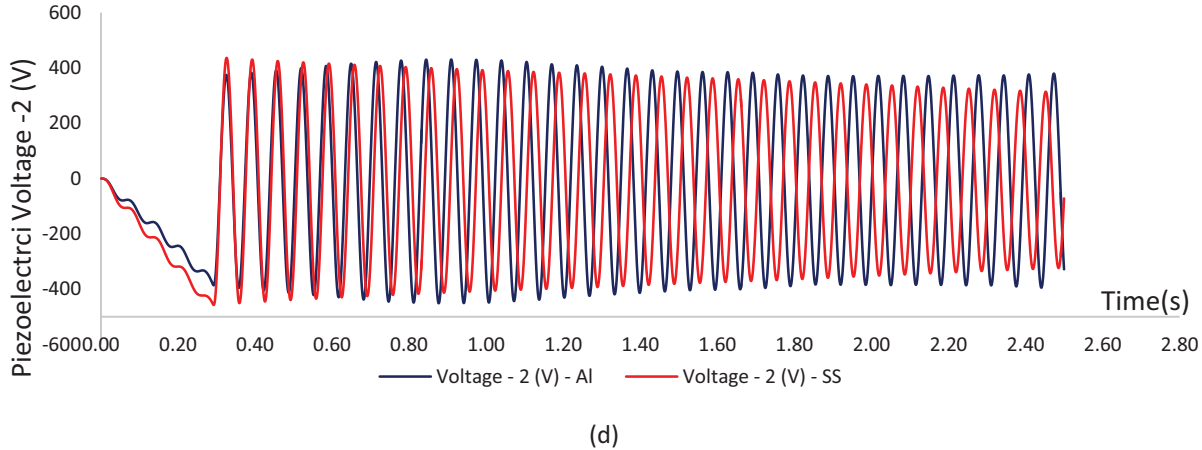


(b)



(c)

Figure 3.11: Variation of parameters for different materials at 23m/s, (a) Tip displacement, (b) Maximum strain, (c) Piezoelectric voltage from piezo body-1, (d) Piezoelectric voltage from piezo body-2 (continued)



(d)

Figure 3.11: Variation of parameters for different materials at 23m/s, (a) Tip displacement, (b) Maximum strain, (c) Piezoelectric voltage from piezo body-1, (d) Piezoelectric voltage from piezo body-2

Figure 3.11(a) shows that the motion of the aluminium harvester does not damp out as opposed to the structural steel harvester. The animations for the stresses for this case have been linked to a Youtube channel, the links of which are [Stress-Al-23m/s](#) and [Stress-SS-23m/s](#). When compared to the laminar wind speed in Figure 3.6, the motion of both harvesters shows an improvement i.e., their motion does not damp out as readily. At a higher wind speed, the motion of each harvester persists for a longer time. This is due to the greater pressure throughout the fluid domain which can be seen from Figure 3.7. The aluminium harvester shows a non-damping motion which is exactly what is desired in the small energy harvester. Due to the strength of structural steel and its resistance to deformation, as is evident from Figure 3.11(a), the structural steel harvester motion dampens over time. In either case i.e. for the laminar or the turbulent wind speed, there is a considerable amount of voltage generated and goes as high as 427 Volts. This voltage is being generated by both piezoelectric bodies attached to the harvester plate on either side. The voltage generated from this harvester can be used to power small devices such as wireless sensors or actuators.

Chapter 4 : Conclusion and Future Work

The computational modeling of the small energy harvester is carried out. The fluid-structure interaction of the harvester i.e. its interaction with a certain wind speed is studied as part of the computational modeling. This property of responding to aero-elastic instabilities is further used to generate a voltage that can be further used to power small energy consuming devices such as wireless sensors and actuators. The modeling of two harvesters made of different materials, namely aluminium and structural steel, is carried out to study their fluid-structure interaction and consequently determine the net voltage generated from each harvester. The modeling is carried out at two distinct wind speeds corresponding to laminar and turbulent flow. The boundary conditions for all cases are kept the same. Only the wind speed is varied and depending on the wind speed it is judged whether the Spalart-Allmaras turbulence model be used.

For the laminar cases, the oscillatory motion of both the harvesters dampens out. However, the aluminium energy harvester dampens slower than the structural steel energy harvester. This is due to the greater strength of structural steel and its ability to withstand the aero-elastic instabilities. Depending on the strain produced in the piezo bodies, a voltage is generated across each piezo body. In order to produce voltage for a longer duration of time, it is required that we design our harvester in such a way such that its motion does not damp out readily. Thus, in the two harvesters being compared, the aluminium harvester is a better choice while operating in regions with laminar flow conditions.

For the turbulent cases, the oscillatory motion of the structural harvester shows promise when compared to the laminar case. The structural steel harvester does not dampen out as readily as in the laminar case. However, in case of the aluminium harvester, the motion does not dampen out and hence, the aluminium harvester produces an alternating but continuous voltage output. This is due to the greater pressure forces experienced by the aluminium harvester in turbulent conditions. From the results and the pressure contours shown, the turbulent cases have a greater pressure developed inside the fluid domain. The strength of the aluminium plate is not

enough to sustain its shape and thus, the motion does not dampen out and the harvester keeps fluttering unlike the structural steel harvester. This is exactly what we desire in the small energy harvester. Thus, the aluminium harvester used in turbulent conditions will give the best voltage output as studied from the computational modeling.

The power extracted from this harvester will depend on the external load circuit that is being used. This provides further opportunities to explore the small energy harvester and serves as a topic of great inter-disciplinary study. Furthermore, the conditions and the geometry of the energy harvester can be changed so as to make it fall under the turbulent Reynolds number limit so that a better voltage output is generated. Also, the properties of the piezoelectric material, the shape of the piezo strips and their dimensions can be changed to study how the voltage output is affected. The harvester needs to be designed using a material that is susceptible to aero-elastic instabilities but does not succumb and fail when operational. Thus, the right material needs to be chosen for the harvester. The square tip prism can be replaced by a different geometry so as to provide a greater instability.

These harvesters are ideal in regions with high wind velocity, the results of which have been incorporated in this study. Further studies may also include simulation of an array of harvesters to determine the net voltage, and consequently, the net power being produced by the complete array. Validation of computational results can be done through wind tunnel testing of the mentioned harvesters. It is the need of the hour to opt for alternative sources of energy to meet the ever increasing energy demands of the world. Countries like Costa Rica have already implemented a 100% clean energy operation over the past months. Using any possible alternative source of energy will not only lessen the burden on conventional energy sources, but will also provide a safer and a cleaner environment to live in. Extensive research in cleaner energy production, however minimal the power output, is a necessity. This study has aimed to tackle exactly that and is a step taken to provide an idea that could aid in the thinking process to move to cleaner energy sources.

References

- [1] Wang, D. A., Chiu, C. Y., Pham, H. T., "Electromagnetic Energy Harvesting from Vibrations induced by Kármán Vortex Street", *Journal of Mechatronics*, Vol. 22(6), pp. 746-756, 2012.
- [2] Park, J., Morgenthal, G., Kim, K., Kwon, S.D., Law, K.H., "Power Evaluation of Flutter-based Electromagnetic Energy Harvesters using Computational Fluid Dynamics Simulations", *Journal of Intelligent Material Systems and Structures*, Vol. 25(14), pp. 1800-1812, 2014.
- [3] Taylor, G. W., Burns, J. R., Kammann, S. M., Powers, W. B., Welsh, T. R., "The Energy Harvesting Eel: A Small Subsurface Ocean/River Power Generator", *IEEE Journal of Oceanic Engineering*, Vol. 26(4), 2001.
- [4] Liya, Z., Lihua, T., Yaowen, Y., "Small Wind Energy Harvesting from Galloping using Piezoelectric Materials", *Proceedings of the ASME 2012 Conference on Smart Materials, Adaptive Structures and Intelligent Systems*, 2012.
- [5] Sundararajan, V., Romero, E., Bonilla, N., Martínez, C., "Energy Harvesting from Fluttering Membranes", *Tenth LACCEI Latin American and Caribbean Conference*, Panama City, Panama, 2012.
- [6] Abdelkefi, A., Hasanyan, A., Montgomery, J., Hall, D., Hajj, M. R., "Incident Flow Effects on the Performance of Piezoelectric Energy Harvesters from Galloping Vibrations", *Theoretical and Applied Mechanics Letters* 4, 2014.
- [7] Ali, M., Arafa, M., Elaraby, M., "Harvesting Energy from Galloping Oscillations", *Proceedings of the World Congress on Engineering*, Vol. 3, 2013.

- [8] Kwon, S.D., "A T-shaped Piezoelectric Cantilever for Fluid Energy Harvesting", *Applied Physics Letters*, 97, 2010.
- [9] Bryant, M., Garcia, E., "Modeling and Testing of a Novel Aero-elastic Flutter Energy Harvester", *ASME Journal of Vibration and Acoustics*, 133(1), pp. 011010-011010-11, 2011.
- [10] Gallina, M., and Benasciutti, D., "Finite Element Analysis of Optimized Piezoelectric Bimorphs for Vibrational Energy Harvesting", *International CAE Conference*, 2013.
- [11] Spalart, P.R., and Allmaras, S.R., "A One-Equation Turbulence Model for Aerodynamic Flows", *30th AIAA Aerospace Sciences Meeting and Exhibit*, Reno, Nevada, USA, 1992.
- [12] Hou, G., Wang, J., Layton, A., "Numerical Methods for Fluid-Structure Interaction – A Review", *Communications in Computational Physics*, Vol. 12(2), pp. 337-377, 2012.
- [13] Baek, H., and Karniadakis, G. E., "A Convergence Study of a New Partitioned Fluid–Structure Interaction Algorithm based on fictitious mass and damping", *Journal of Computational Physics*, 231, pp. 629–652 (2012).
- [14] C. Wood, A.J. Gil, O. Hassan, J. Bonet, "Partitioned Block-Gauss–Seidel Coupling for Dynamic Fluid–Structure Interaction", *Journal of Computers and Structures*, 88, pp. 1367–1382, 2010.
- [15] Farhat, C., and Lesoinne, M., "Two Efficient Staggered Algorithms for the Serial and Parallel Solution of Three-Dimensional Nonlinear Transient Aero-elastic problems", *Computer Methods in Applied Mechanics and Engineering*, 182, pp. 499-515, 2000.
- [16] *IEEE Standard on Piezoelectricity*, ANSI/IEEE, Std. 176, 1987.

- [17] Sirohi, J., Chopra, I., "Fundamental Understanding of Piezoelectric Strain Sensors", *Journal of Intelligent Material Systems and Structures*, Vol. 11(4), pp. 246-257, 2000.
- [18] Kim, K., Lee, S., Kwon, S. D., "Wind Energy Harvesting from Aero-elastic Instability", *The Eighth Asia-Pacific Conference on Wind Engineering*, Chennai, India, 2013.
- [19] Erturk, A., Inman, D. J., "Piezoelectric Energy Harvesting", *John Wiley and Sons Ltd.*, First Edition, ISBN: 978-0-470-68254-8, pp. 373-374, 2011.
- [20] Roache, P. J., "Verification and Validation in Computational Science and Engineering", *Hermosa Publishers, Albuquerque, New Mexico*, 1998.

Appendix

The animations pertaining to the cases studied in the report are uploaded to a Youtube channel, the links of which are as follows:

1. [Pressure-Al-9m/s](https://www.youtube.com/watch?v=S_zioxmrgjc)
2. [Velocity-Al-9m/s](https://www.youtube.com/watch?v=QED6xNYsTS0)
3. [Vorticity-Al-9m/s](https://www.youtube.com/watch?v=ijnUa0-mlIM)
4. [Stress-Al-9m/s](https://www.youtube.com/watch?v=kD0Z2X8RVes)
5. [Pressure-SS-9m/s](https://www.youtube.com/watch?v=wiYyZIM4jCg)
6. [Velocity-SS-9m/s](https://www.youtube.com/watch?v=YljowZBq7BY)
7. [Vorticity-SS-9m/s](https://www.youtube.com/watch?v=LLszID1mXic)
8. [Stress-SS-9m/s](https://www.youtube.com/watch?v=ewy2TZR7k_4)
9. [Pressure-Al-23m/s](https://www.youtube.com/watch?v=yCNfgxHKbDw)
10. [Velocity-Al-23m/s](https://www.youtube.com/watch?v=XA54T94x-Po)
11. [Vorticity-Al-23m/s](https://www.youtube.com/watch?v=lsWW_0cuDCo)
12. [Stress-Al-23m/s](https://www.youtube.com/watch?v=oPyLO361oNM)
13. [Pressure-SS-23m/s](https://www.youtube.com/watch?v=FHO-8u1vkYQ)
14. [Velocity-SS-23m/s](https://www.youtube.com/watch?v=f6CEdwUWgM8)
15. [Vorticity-SS-23m/s](https://www.youtube.com/watch?v=6kluiDy46x4)
16. [Stress-SS-23m/s](https://www.youtube.com/watch?v=jRCs64p06Pw)